Geochemistry
Geophysics
Geosystems
$G^3$

*Article*
Volume 13, Number 1
18 January 2012
Q01010, doi:10.1029/2011GC003860
ISSN: 1525-2027

Published by AGU and the Geochemical Society

# Fluid flow during slab unbending and dehydration: Implications for intermediate-depth seismicity, slab weakening and deep water recycling

**Manuele Faccenda**
*School of Mathematical Sciences, Monash University, Clayton, Victoria 3800, Australia (manuele.faccenda@gmail.com)*

**Taras V. Gerya**
*Geophysical Fluid Dynamics, Institute of Geophysics, ETH Zürich, Sonneggstrasse 5, Zurich CH-8092, Switzerland*

**Neil S. Mancktelow**
*Institute of Geology, ETH Zürich, Sonneggstrasse 5, Zurich CH-8092, Switzerland*

**Louis Moresi**
*School of Mathematical Sciences, Monash University, Clayton, Victoria 3800, Australia*

[1] Subducting oceanic plates carry a considerable amount of water from the surface down to mantle depths and contribute significantly to the global water cycle. A part of these volatiles stored in the slab is expelled at intermediate depths (70–300 km) where dehydration reactions occur. However, despite the fact that water considerably affects many physical properties of rocks, not much is known about the fluid flow path and the interaction with the rocks through which volatiles flow in the slab interior during its dehydration. We performed thermomechanical models (coupled with a petrological database and with incompressible aqueous fluid flow) of a dynamically subducting and dehydrating oceanic plate. Results show that, during slab dehydration, unbending stresses drive part of the released fluids into the cold core of the plate toward a level of strong tectonic under-pressure and neutral (slab-normal) pressure gradients. Fluids progressively accumulate and percolate updip along such a layer forming, together with the upper hydrated layer near the top of the slab, a Double Hydrated Zone (DHZ) where intermediate-depth seismicity could be triggered. The location and predicted mechanics of the DHZ would be consistent with seismological observations regarding Double Seismic Zones (DSZs) found in most subduction zones and suggests that hydrofracturing could be the trigger mechanism for observed intermediate-depth seismicity. In the light of our results, the lower plane of the DSZ is more likely to reflect a layer of upward percolating fluid than a level of mantle dehydration. In our models, a 20–30 km thick DSZ forms in relatively old oceanic plates without requiring an extremely deep slab hydration prior to subduction. The redistribution of fluids into the slab interior during slab unbending also has important implications for slab weakening and the deep water cycle. We estimate that, over the whole of Earth's history, a volume of water equivalent to around one to two oceans can be stored in nominally anhydrous minerals of the oceanic lithosphere and transported to the transition zone by this mechanism, suggesting that mantle regassing could have been efficient even without invoking the formation of high pressure hydrous minerals.

**Components:** 10,700 words, 13 figures, 2 tables.

**Keywords:** fluid flow; intermediate-depth earthquakes; slab dehydration; slab weakening.

**Index Terms:** 3612 Mineralogy and Petrology: Reactions and phase equilibria (1012, 8412); 3613 Mineralogy and Petrology: Subduction zone processes (1031, 3060, 8170, 8413); 3653 Mineralogy and Petrology: Fluid flow.

**Received** 7 September 2011; **Revised** 5 December 2011; **Accepted** 6 December 2011; **Published** 18 January 2012.

Faccenda, M., T. V. Gerya, N. S. Mancktelow, and L. Moresi (2012), Fluid flow during slab unbending and dehydration: Implications for intermediate-depth seismicity, slab weakening and deep water recycling, *Geochem. Geophys. Geosyst.*, *13*, Q01010, doi:10.1029/2011GC003860.

## 1. Introduction

[2] Water is the most important volatile component of silicate rocks because it significantly reduces their strength [*Karato and Wu*, 1993; *Katayama and Karato*, 2008; *Mei and Kohlstedt*, 2000], enhances electrical conductivity [*Wang et al.*, 2006], favors partial melting [*Kushiro et al.*, 1968] and may trigger deep seismicity [*Raleigh and Paterson*, 1965]. Placing better constraints on the distribution and transport of this critical volatile component is therefore very important for understanding the dynamics of our planet.

[3] Seawater is transported into the mantle by oceanic plates that are hydrated before being subducted. In fact, several geophysical studies indicate that 10–20 km of the upper part of the subducting oceanic slabs are hydrated at trenches [*Contreras-Reyes et al.*, 2011; *Ivandic et al.*, 2010; *Ranero et al.*, 2003; *Ranero and Sallares*, 2004]. This oceanic plate hydration has been proposed to occur at mid-ocean ridges [*Ranero et al.*, 2003], due to hot spot magmatism [*Seno and Yamanaka*, 1996], or as the result of bending-related normal faulting at the trench outer rise [*Faccenda et al.*, 2009; *Ranero et al.*, 2003]. As the oceanic plate descends into the upper mantle, it progressively heats up, leading to the breakdown of hydrous minerals that release silica-rich fluids [e.g., *Hacker et al.*, 2003; *Peacock*, 2001]. The observed intermediate-depth (70–300 km) seismicity is normally interpreted as due to such slab dehydration [*Kirby et al.*, 1996; *Peacock*, 2001; *Yamasaki and Seno*, 2003]. However, if the oceanic plate is old enough, some low-pressure hydrous phases (e.g., antigorite) are transformed into high-pressure hydrous (DHMS) phases that are stable down to the base of the upper mantle [*Ohtani*, 2005]. This appears to be a very efficient mechanism for mantle regassing, occurring especially at levels that have high water solubility, such as the transition zone (3 wt% [*Bercovici and Karato*, 2003]).

[4] In the past few years, numerical modeling has been extensively used to simulate subduction zones processes related to the presence of bound and/or free volatiles. Thermal models coupled with petrological databases have explored the stability of hydrous phases in subducting slabs in order to estimate mantle regassing [*Rüpke et al.*, 2004; *van Keken et al.*, 2011] and to reconcile the observed intermediate-depth earthquakes with dehydration reactions [*Hacker et al.*, 2003; *Peacock*, 2001; *Yamasaki and Seno*, 2003]. It has been found that (1) during the whole Earth's history around 1 ocean mass of $H_2O$ has been subducted into the upper mantle and (2) because the distribution of the hypocenters resembles the stability field of major hydrous phases plotted on the slab, dehydration embrittlement may effectively be responsible for the observed seismicity. Thermomechanical models that account for incompressible fluid flow and phase transformations have investigated the migration of volatiles mainly in the mantle wedge [*Cagnioncle et al.*, 2007; *Gerya and Yuen*, 2003; *Gorczyk et al.*, 2007; *Hebert et al.*, 2009; *Spiegelman and McKenzie*, 1987]. However, no numerical experiment has so far explored the fluid flow in the slab associated with its dehydration at intermediate-depths and the interaction of the volatiles with the solid matrix through which they flow. This is because the common assumption is that fluids are expelled toward the mantle wedge due to the vertically decreasing pressure, although it has been suggested that part of the released $H_2O$ may migrate updip along the slab [*Hacker et al.*, 2003].

[5] Recent studies have recognized that, at depths where the pore fluid pressure approaches the solid pressure, fluid flow is driven mainly by gradients in tectonic stresses causing deformation [e.g., *Connolly and Podladchikov*, 2004; *Faccenda et al.*, 2009; *Katz et al.*, 2006; *Mancktelow*, 2008]. For instance, *Faccenda et al.* [2009] showed that during plate

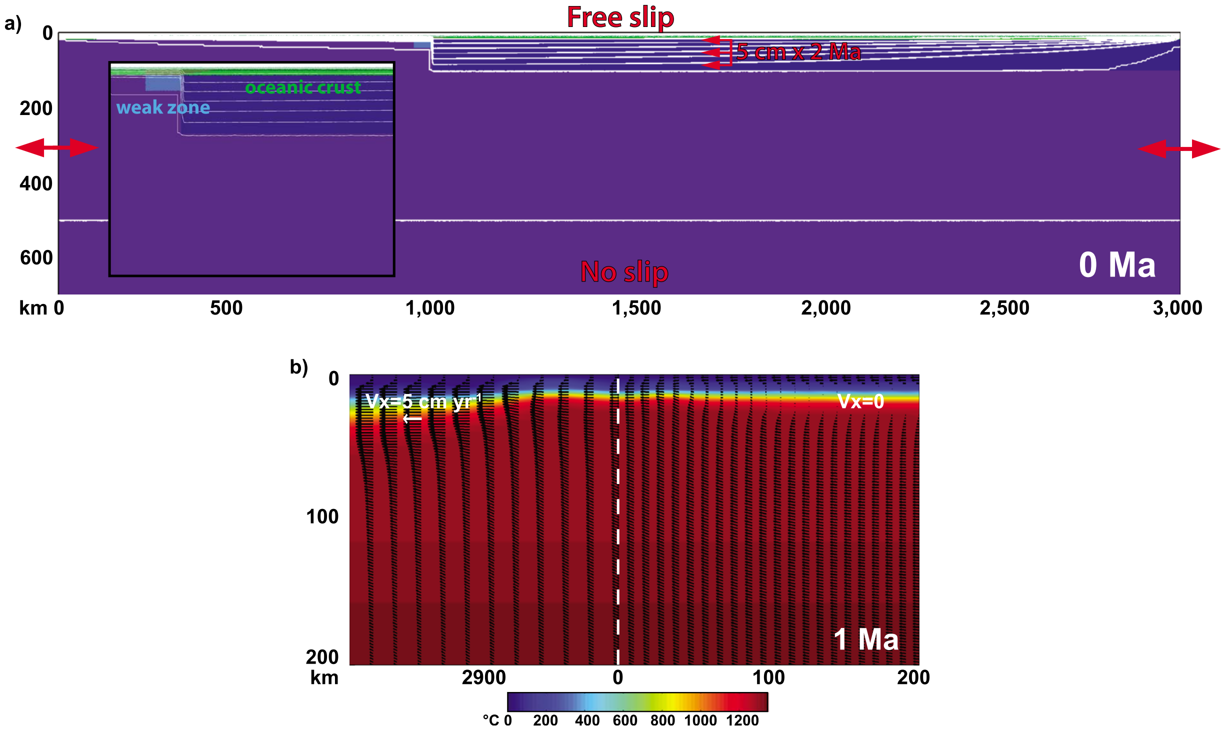

**Figure 1.** (a) Initial model geometry and boundary conditions. Color scale as in Figure 3. White lines are isotherms. The inset shows the hydrated transform margin where subduction is initiated. The arrows on the right and older plate show the place where a convergence rate of 5 cm/year is imposed for the first 2 Ma. Double arrows on the vertical margins indicate periodic boundary conditions. (b) Thermal (in color) and solid velocity vector (arrow) fields across the vertical, periodic boundaries. The solution is computed at 1 Ma when the kinematic boundary conditions are imposed. The older plate is moving rightward at constant rate of 5 cm/yr while the younger plate is blocked along the horizontal direction.

bending strong variation of the tectonic pressure (equal to the difference between the total pressure and the lithostatic pressure in the solid rock matrix) favors downward fluid flow in the subducting slab. During slab dehydration at intermediate depths, the pore fluid pressure is certainly close to the solid pressure [e.g., *Gerya et al.*, 2008, and references therein] and the strong gradients in tectonic pressure induced by slab unbending [e.g., *Babeyko and Sobolev*, 2008; *Dorbath et al.*, 2008] could significantly affect the fluid flow. Using simple 1D models of slab bending and unbending, *Faccenda and Mancktelow* [2010] argued that slab-normal, sub-hydrostatic pressure gradients that should always develop in the unbending slab lithosphere could potentially drive fluids slab inward toward the slab core.

[6] In this paper we present the results of thermo-mechanical models of subducting oceanic plates, specifically considering the effects of hydration/dehydration reactions in the oceanic lithosphere and of incompressible fluid flow. We show that modeling fluid flow in the slab after its dehydration has important implications for the observed intermediate-depth seismicity, the global water cycle and the slab rheology.

## 2. Numerical Modeling

### 2.1. Thermomechanical and Fluid Flow Modeling

[7] The numerical experiments were carried out with I2ELVIS [*Gerya and Yuen*, 2007], a finite difference, particle-in-cell code that accounts for incompressible two-phase flow and visco-elasto-plastic deformation of the solid matrix. The initial model geometry is similar to previous studies of *Faccenda et al.* [2008, 2009] and is shown in Figure 1a. The models use variable grid spacing in the horizontal direction, gradually increasing from 2 km close to the trench (±300 km) to a maximum of ~8 and ~20 km on the left and right boundaries, respectively. To continually resolve the subduction process, the horizontal grid resolution moves with the trench position. The grid spacing in the vertical direction is 2 km.

**Table 1.** Parameters Description

| Variable | Description | Constant Value Used | Dimension |
|---|---|---|---|
| $\Phi$ | Porosity | 0.01 | |
| K | Permeability | $10^{-18}$ | $m^2$ |
| $v_s$, $v_f$ | Solid, fluid velocity vector | -, - | $m\ s^{-1}$ |
| $\rho_s$ | Solid density | see Table 2 | $kg\ m^{-3}$ |
| $\rho_f$ | Fluid density | 1000 | $kg\ m^{-3}$ |
| $\eta_s$ | Visco-elasto-plastic solid shear viscosity | see Table 2 | Pa s |
| $\eta_f$ | Fluid shear viscosity | $10^{-4}$ | Pa s |
| G | Gravity vector | $g_x = 0$; $g_z = 9.81$ | $m\ s^{-2}$ |
| $P_s$ | Solid pressure | - | Pa |
| $P_{lith}$ | Lithostatic pressure | - | Pa |
| $P_{tect} = P_s - P_{lith}$ | Tectonic pressure | - | Pa |
| $\bar{P}_f$ | Non-hydrostatic (piezometric) fluid pressure | - | Pa |
| T | time | - | s |
| Z | Depth | - | m |
| $z_L$ | Oceanic lithosphere thickness (equation (1)) | 90 | km |
| $T_0$ | Plate surface temperature (equation (1)) | 273 | K |
| $T_1$ | Plate temperature at $z_L$ (equation (1)) | 1573 | K |
| K | Thermal diffusivity (equation (1)) | $10^{-6}$ | $m^2\ s^{-1}$ |
| K | Solid thermal conductivity | see Table 2 | $W\ m^{-1}\ K^{-1}$ |
| Cp | Solid heat capacity | 1000 | $J\ kg^{-1}\ K^{-1}$ |
| A | Solid thermal expansion | $3 \times 10^{-5}$ | $K^{-1}$ |
| B | Solid compressibility | $1 \times 10^{-5}$ | $MPa^{-1}$ |
| G | Shear modulus | see Table 2 | GPa |
| C | Cohesion | 1 | MPa |
| $\sin\varphi_{\mathbf{strong}}$ | Friction angle at $\varepsilon_{brittle} = 0$ (equation (2)) | see Table 2 | - |
| $\sin\varphi_{\mathbf{weak}}$ | Friction angle at $\varepsilon_{brittle} \geq \varepsilon_{brittle\_weak}$ (equation (2)) | see Table 2 | - |
| $\varepsilon_{brittle}$ | Brittle finite strain (equation (2)) | - | - |
| $\varepsilon_{brittle\_weak}$ | Brittle finite strain threshold for maximum plastic weakening (equation (2)) | 1 | - |
| $\varepsilon_{brittle\_serp}$ | Brittle finite strain threshold for serpentinization | 0.02 | - |
| $NAM_{H2O}$ | Water content of nominally anhydrous minerals | 1000–2000 | wt ppm |

[8] The plates thermal structure is calculated using a cooling plate model that gives an empirically good fit to seafloor subsidence for plates older than 70–80 Ma [*Carslaw and Jaeger*, 1984] (see Table 1 for an explanation of symbols):

$$T = T_0 + (T_1 - T_0)\left[\frac{z}{z_L} + \frac{2}{\pi}\sum_{n=1}^{\infty}\frac{1}{n}\exp\left(-\frac{kn^2\pi^2 t}{z_L^2}\right)\sin\left(\frac{n\pi z}{z_L}\right)\right] \tag{1}$$

The age of the plates decreases linearly toward the left and right boundaries, which correspond to mid-ocean ridges. Both younger (1 Ma) and older (30–150 Ma) plates are considered in different models.

[9] Rheological and thermal parameters used in the models are listed in Table 2. Brittle weakening of the solid rocks is linearly dependent on the brittle/plastic finite strain ($\varepsilon_{brittle}$) according to

$$\sin\varphi = \sin\varphi_{strong} + \left(\sin\varphi_{weak} - \sin\varphi_{strong}\right)\frac{\varepsilon_{brittle}}{\varepsilon_{brittle\_weak}} \tag{2}$$

where $\sin\varphi$, $\sin\varphi_{strong}$ and $\sin\varphi_{weak}$ are the computed, the initial and the minimum value of the

**Table 2.** Solid Material Properties

| Rock Type | $\rho_s$ | $k^a$ | Flow Law$^b$ | G | $\sin\varphi_{\mathbf{strong}}$ | $\sin\varphi_{\mathbf{weak}}$ |
|---|---|---|---|---|---|---|
| Basaltic crust | 3300 | $1.18 + \frac{474}{T+77}$ | Wet Quartzite | 25 | 0 | 0 |
| Gabbroic crust | 3300 | $1.18 + \frac{474}{T+77}$ | Plagioclase $An_{75}$ | 25 | 0.5 | 0.4 |
| Lithosphere-astenosphere dry mantle | 3300 | $0.73 + \frac{1293}{T+77}$ | Dry Olivine | 67 | 0.5 | 0.4 |
| Hydrated mantle | 3300 | $0.73 + \frac{1293}{T+77}$ | Wet Olivine | 25 | 0.5 | 0.4 |
| Serpentinized mantle | 3200 | $0.73 + \frac{1293}{T+77}$ | Wet Olivine | 25 | 0.3 | 0.3 |

[a] *Clauser and Huenges* [1995].
[b] Flow laws are from *Ranalli* [1995].

coefficient of friction appropriate for the Drucker-Prager plastic yield criterion, as used in the models, where $\varphi$ is the corresponding angle of friction. The minimum coefficient of friction ($\sin\varphi_{weak}$) is established for plastic finite strains $\varepsilon_{brittle} \geq \varepsilon_{brittle\_weak} = 1$ for all the lithologies.

[10] Subduction is initiated at a weak (wet olivine rheology) transform margin. A constant convergence velocity of 5 cm/yr is applied to the older plate at 1750 km while the horizontal velocity of the younger plate is set to zero from 100 to 760 km for the first 2 Ma, after which the model evolves dynamically. The Boussinesq approximation is used. The computational domain is periodic in the horizontal direction, while free slip and no slip boundary conditions are imposed on the upper and lower margins, respectively. Domain periodicity is computed discretizing the equations of conservation of mass, momentum and energy across the vertical margins of the staggered grid according to the finite difference method and setting the horizontal velocities, temperatures and the physical parameters (i.e., shear viscosity, density, thermal conductivity) on the last vertical gridline to be equal to those of the first one. The physical parameters defined on the first vertical gridlines are interpolated from markers sited on the left- and right-most cells. As an example, Figure 1b shows the solution of the temperature and velocity field around the vertical boundaries of the computation domain at 1 Ma when the initial kinematic boundary conditions are imposed.

[11] Fluid-flow is modeled as in the work by *Faccenda et al.* [2009], assuming that the pore fluid pressure is equal to the solid pressure (i.e., to the mean normal stress on solids), that there is no mass and heat transfer between the solid and fluid phases, and using constant hydraulic parameters. With such assumptions, the full two-phase flow equations reduce to an incompressible Stokes flow for the solid phase while the fluid flow is driven by the piezometric pressure gradients (see Appendix A).

[12] In contrast, real two-phase flow systems are characterized by substantial variations in the solid matrix porosity during chemical reactions (for example, dehydration of serpentine implies a negative volume change at intermediate depths [*Jung et al.*, 2004]), causing mechanical compaction/decompaction that generates additional, non-divergent solid flow. The simplified approach we have adopted here is considered to be appropriate to the modeled system, because fluid flow along the cold core of the slab occurs with elasto-plastic deformation of the solid matrix and with only negligible viscous flow, due to the low temperatures and strain rates (and consequently, for power law behavior, high effective viscosities) involved. Accounting for full visco-elasto-plastic two-phase flow is beyond the scope of the current paper and would require considerable amount of code benchmarking and model testing since little has been previously done in this direction. The implications that arise from the results of our calculations are indeed potentially affected by uncertainties inherent in our simplifying assumptions for modeling fluid flow (Appendix A). However, we consider that simplified formulation employed should still reproduce to first order fluid flow behavior in the subducting slab for the following reasons:

[13] 1. Whenever free fluid in excess is present at depth, it will be associated by definition with some degree of porosity, irrespective of how much compaction or solid volume increase take place. If this porosity is not connected to the surface, as is the case at intermediate depths, the fluid pressure will be close to the solid pressure ($P_f \cong P_s$), so that fluids will be able to establish transient paths along grain boundaries and elasto-plastic cracks driven by the solid pressure gradients.

[14] 2. Any mechanism that produces a porosity reduction (like compaction or solid volume increase associated with hydration reactions) would slow down the fluid flow but it would also increase the fluid pressure, leading eventually to hydrofracturing and thus to fluid flow along the newly created porous network. Conversely, an increase of porosity would enhance permeability and thereby promote fluid flow but, on the other hand, it would also lower the piezometric pressure and the associated Darcyan velocity. Hence, for a given solid pressure gradient, the time-integrated rate at which free fluids flow in elasto-plastic media should be rather constant.

[15] The constant porosity and permeability used in the models are taken to represent the long-term hydraulic properties of the slab averaged over time through the various phases of elasto-plastic compaction and decompaction. In this averaging, any change of porosity/permeability is buffered by an associated change of fluid pressure and the rate at which fluid-filled cracks migrate in the slab, facilitating fluid migration, are considered to mainly depend on the magnitude of the solid pressure gradients.

## 2.2. Hydration and Dehydration Modeling

[16] The 8 km thick oceanic crust is initially hydrated homogeneously (chemically bound water: 4 wt% for 2 km of basaltic upper crust and 1.4 wt%

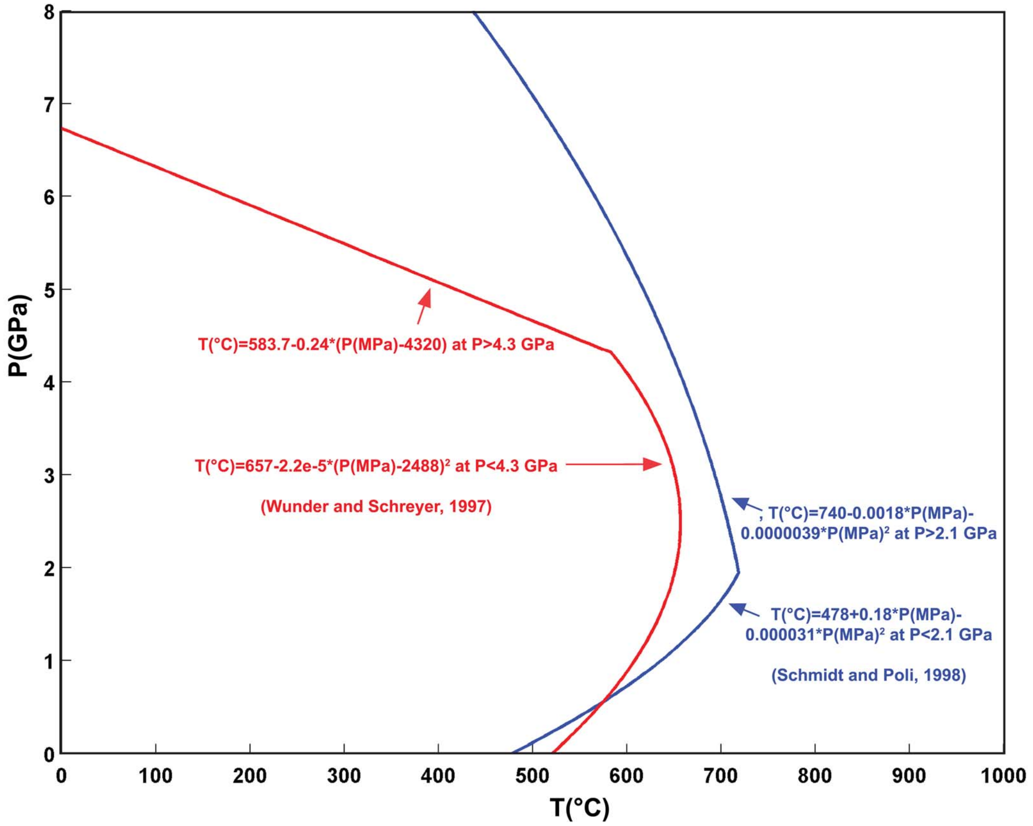

**Figure 2.** Antigorite dehydration curves taken from *Schmidt and Poli* [1998] (blue curve) and *Wunder and Schreyer* [1997] (red curve).

for 6 km of gabbroic lower crust at the surface), while slab mantle serpentinization at the trench is set to occur down to a maximum sub-Moho depth of 5–10 km (13–18 km from the slab surface) for different models in response to bending-related brittle normal faulting as in the work by *Faccenda et al.* [2008]. When the lithospheric mantle exceeds a threshold finite brittle deformation ($\varepsilon_{\text{brittle\_serp}} = 0.02$), the material particle is transformed into a serpentinized rock that, at these P-T conditions, contains about 2 wt% of bound water (15% of serpentinization). This value is representative of the average degree of serpentinization estimated at trenches from tomographic studies such as, for example, in the upper 5–10 km of the Cocos plate lithospheric mantle [*Ivandic et al.*, 2010; *Van Avendonk et al.*, 2011]. This approach allows the extent and pattern of lithospheric mantle hydration to be established with a relatively low (2 km) numerical resolution in contrast to the high spatial resolution (0.5 km) study of fault serpentinization by *Faccenda et al.* [2009] which in the current models would involve a very high computational cost. At intermediate-depths, in contrast, where plastic behavior is not active, serpentinization of the cold slab interior occurs intrinsically in the models as a result of reaction between fluids in excess and the dry rocks through which they migrate.

[17] The water content of hydrated rocks and the dehydration reactions that occur in the oceanic crust are computed with PERLPLE_X [*Connolly*, 2005]. A discontinuous reaction is used for antigorite dehydration according to the stability fields drawn in Figure 2 (hereafter the antigorite dehydration curves are denominated SP1998 if taken from *Schmidt and Poli* [1998] and WS1997 if taken from *Wunder and Schreyer* [1997]). At P-T conditions where antigorite is stable, the water content is that of a hydrated mantle peridotite. Conversely, when antigorite is no longer stable, the material particle is transformed into wet peridotite (i.e., nominally anhydrous minerals). Because a complete database for nominally anhydrous minerals at high confining pressures is not yet available, the water content of these phases ($NAM_{H2O}$) is set to a constant value of either 1000 or 2000 wt ppm in various models [*Bolfan-Casanova*, 2005; *Mainprice*, 2007]. We do not take into account the phase change of antigorite into high-pressure

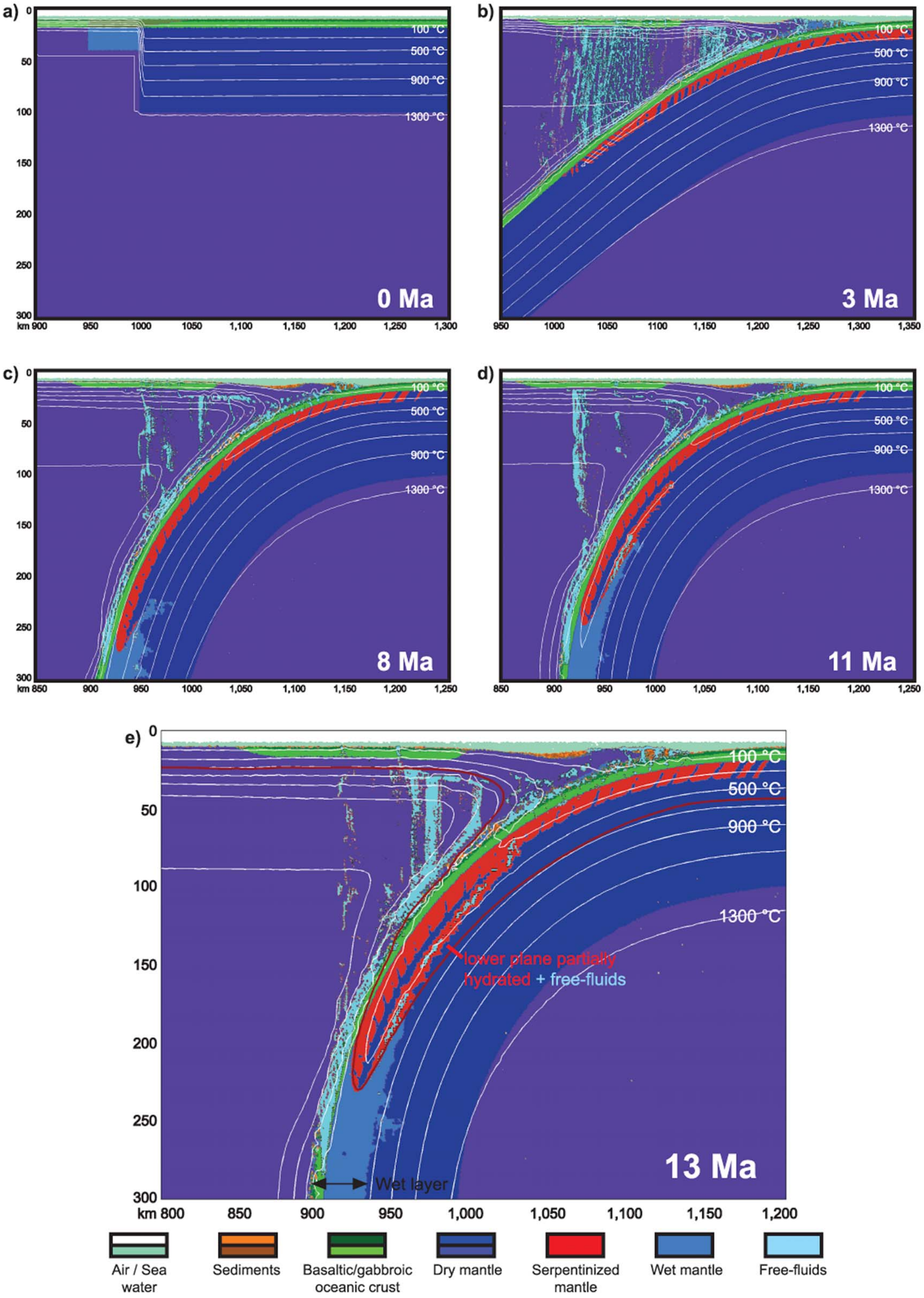

**Figure 3.** Snapshots of the reference model. Fluid concentration and plate re-hydration occur in a mid-lithospheric mantle layer (500 ± 50°C). In Figure 3e the subducting slab is 52 Ma old at depths where the DSZ forms. Dehydration of the oceanic crust occurs over a broad range of pressure and temperature conditions according to the implemented thermodynamic database. The free-fluids present in the lower plane of the DHZ are water in excess because the mantle rocks are saturated in bound-$H_2O$ to the assumed upper serpentinization limit (2 wt %). The dark red line is SP1998. White lines are isotherms.

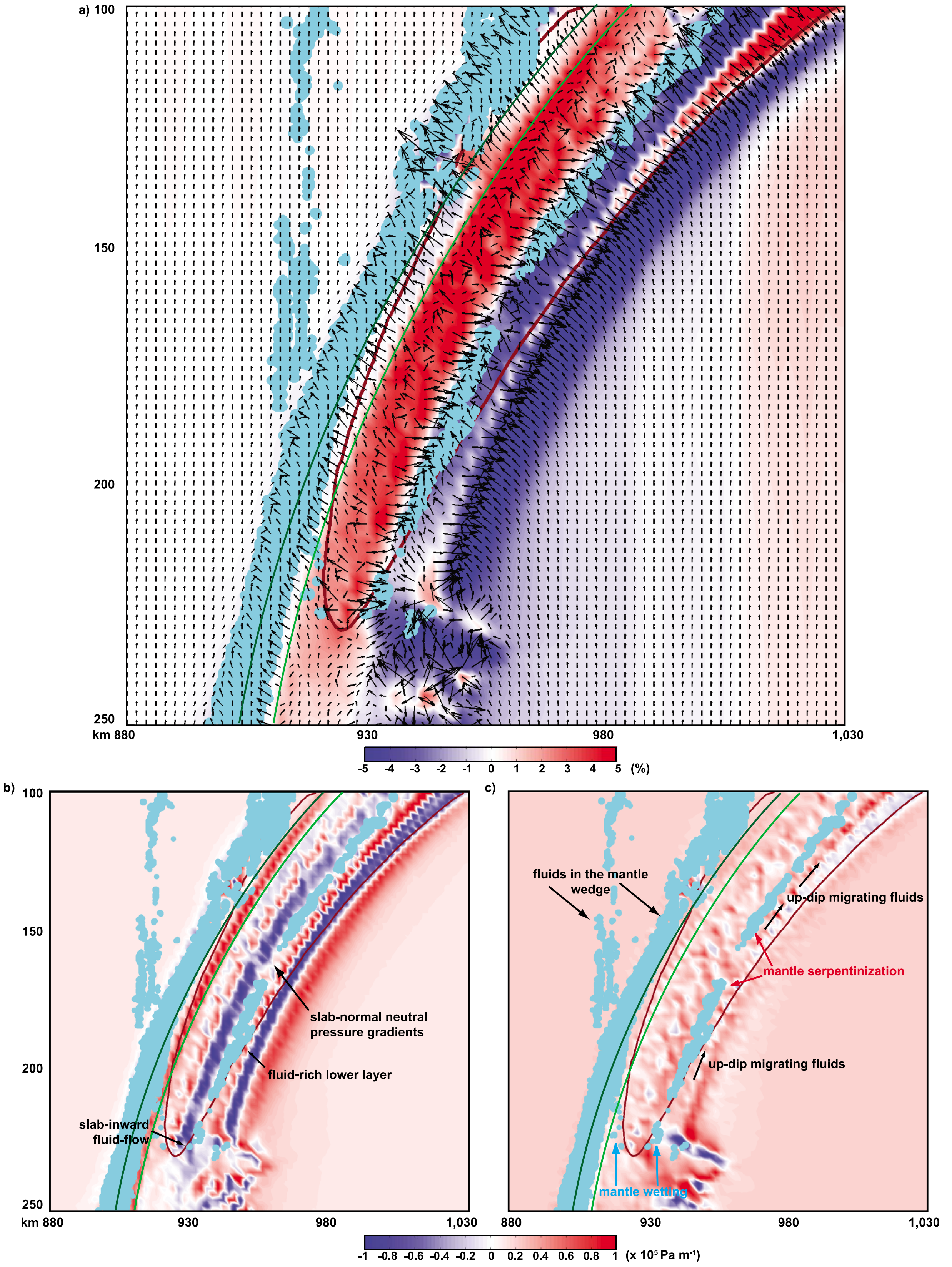
a) 100
150
200
250
km 880
930
980
1,030
-5 -4 -3 -2 -1 0 1 2 3 4 5 (%)
b) 100
150
200
250
km 880
930
980
1,030
slab-normal neutral pressure gradients
fluid-rich lower layer
slab-inward fluid-flow
c)
880
930
980
1,030
fluids in the mantle wedge
up-dip migrating fluids
mantle serpentinization
up-dip migrating fluids
mantle wetting
-1 -0.8 -0.6 -0.4 -0.2 0 0.2 0.4 0.6 0.8 1 (x 10⁵ Pa m⁻¹)

**Figure 4**

hydrous (DHMS) phases [e.g., *Ohtani*, 2005]. For simplicity, hydration/serpentinization at depth is allowed only for lithospheric rocks, and melting is not considered.

[18] The fluid mass is conserved through the different hydration/dehydration reactions in the following way: a fluid particle is created where the difference between the water content of a solid particle and that predicted by PERLPE_X or by the $NAM_{H2O}$ imposed by us exceeds 1000 wt ppm (this value is chosen to avoid the formation of too many fluid markers that will affect negatively the computational performance). The fluid particle water content is then the calculated water in excess. Conversely, if a fluid marker is in proximity to a solid particle whose water content is lower than that predicted by PERLPE_X (i.e., during hydration), the water of the fluid marker is consumed till saturation of the solid marker or until the fluid in excess is consumed (leading to fluid marker deletion).

## 3. Results

### 3.1. Reference Model

[19] The full evolution of the reference model (70–0 Ma old subducting slab) can be seen in Animations S1 and S2 (see Figure 3 for explanation of the color scale).[1] At a mature stage of subduction (>10 Ma), the oceanic crust dehydrates continuously [e.g., *Schmidt and Poli*, 1998] over a range of depths from 20 to less than 300 km, while serpentinized mantle decomposes between 200 and 250 km depth. Fluids produced by the breakdown of hydrous phases then migrate according to the solid pressure gradients. As recognized in previous studies [*Babeyko and Sobolev*, 2008; *Dorbath et al.*, 2008], slab unbending mainly driven by the slab pull occurs at depths of 150 to 300 km, which results in the continuous straightening of the downgoing subducted slab portion that was previously bent at shallow depths in the outer rise region. The unbending induces tectonic over-pressure in the upper part of the slab (mainly focused immediately below the Moho) and tectonic under-pressure at deeper levels (Figure 4a), leading to the formation of fluid over-pressure (supra-hydrostatic) and under-pressure (sub-hydrostatic) gradients in the direction normal to the slab (Figure 4b) and mainly fluid over-pressure gradients in the direction parallel to the slab (Figure 4c). Fluids released from the slightly over-pressurized crust are expelled upward, while those produced by the decomposition of serpentine are driven deeper in a level with strong tectonic under-pressure (Figure 4a) and neutral (slab-normal) pressure gradient (Figure 4b). In fact, the cold and rheologically stronger sub-Moho mantle, where tectonic over-pressure focuses, is a "watershed" acting as a barrier to fluid flow across the slab. During percolation, water is consumed by either crustal and mantle wetting ($NAM_{H2O}$ = 1000 ppm %) or by slab mantle serpentinization at P-T conditions where hydrous phases are stable. Fluids in excess that accumulate in the saturated slab mantle subsequently migrate updip along a planar zone (channel) of neutral (slab-normal, Figure 4b) pressure gradients where antigorite is stable, provided an amount of water sufficient to serpentinize the mantle rocks through which they flow is available. Fluid concentration is however delayed by slab deformation at the 660 km discontinuity, which partly compensates the slab pull and induces tectonic stress fluctuations (supra- and sub-hydrostatic pressure gradients) in the dehydrating regions at 50–250 km depths. As a consequence, an extended (up to 200 km long) hydrated lower plane only forms at a mature (near steady state) stage of subduction (>10 Ma) that, together with the upper hydrated layer, forms what we define as a Double Hydrated Zone (DHZ). Subsequently (>13 Ma), the thickness of the DHZ decreases as progressively younger portions of the downgoing oceanic plate subduct and the upper and lower planes tend to merge.

[20] The fluid velocity is about 1–100 m/year along the slab (depending on the permeability), while it is only a few cm/year in the mantle wedge away from the unbending oceanic plate, where fluids are only driven by lithostatic pressure gradients (Figure S1).

---

[1] Auxiliary materials are available in the HTML. doi:10.1029/2011GC003860.

**Figure 4.** Tectonic pressure and non-hydrostatic (piezometric) fluid pressure gradients in the unbending area. The area corresponds to the central part of Figure 3. (a) Tectonic pressure map. Values are variations (in percentage) of the tectonic pressure relative to the lithostatic load. The black arrows indicate non-hydrostatic fluid pressure gradients ($\nabla \bar{P}_f$) computed on the Eulerian grid (node spacing is 2 km). (b, c) Maps of non-hydrostatic pressure gradient components rotated in the direction normal (Figure 4b) and parallel (Figure 4c) to the slab dip (60°). Blue correspond to sub-hydrostatic pressure gradients, while red indicate supra-hydrostatic gradients. Cyan dots are free-fluid markers. The dark red line is the SP1998. The light and dark green lines are, respectively, the Moho and the top of the gabbroic oceanic crust. The color bar is the same for Figures 4b and 4c.

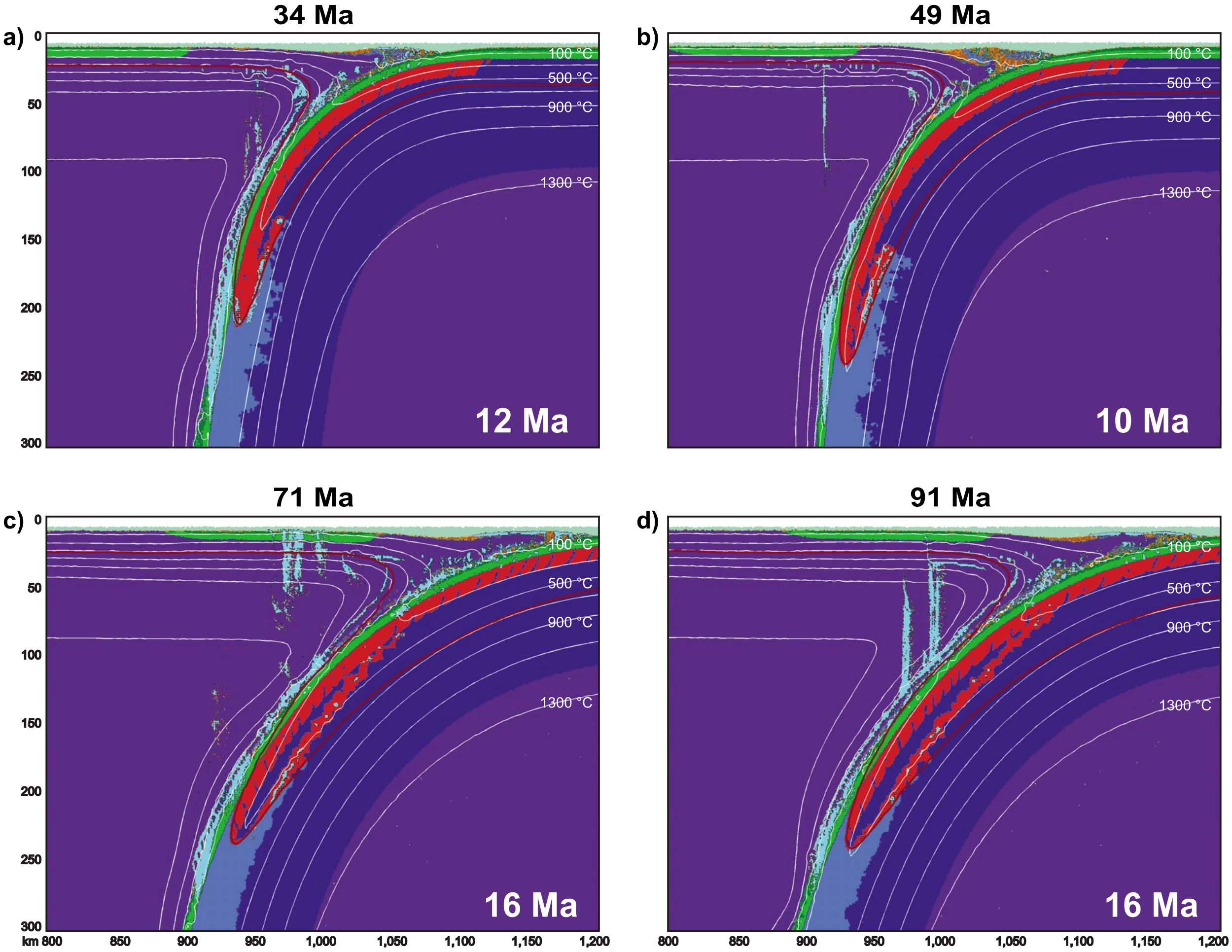

**Figure 5.** Snapshots of numerical models with different ages (in black) of the subducting plate at intermediate depths, with respect to the reference model. The white number in the bottom right of each panel is the time elapsed since the beginning of the numerical experiment. Color scale as in Figure 3. White lines are isotherms. The dark red line is the SP1998.

As expected, the strongest fluid migration rates are established on the boundaries of the high and low tectonic pressure regions, where solid pressure gradients are the greatest. The upward migration rate of fluids is about 0.05–50 m for different permeabilities and at different positions along the lower plane of the DHZ. For a given permeability, the variation of the fluid velocity along the lower plane of the DHZ is a result of the heterogeneous hydration of the slab mantle, which produces an irregular pattern of solid pressure gradients. This explains why the upward fluid percolation along the lower plane of the DSZ seems to be rather sporadic.

[21] The results of the reference model have been tested for various parameters, such as slab age, the antigorite reaction curve, the degree of oceanic lithosphere wetting, the maximum hydration depth in the mantle at trenches, and the numerical resolution.

## 3.2. Different Slab Age

[22] Numerical models with a different age of the subducting plate are shown in Figure 5. Old slabs subduct faster and with a gentler dip compared to young oceanic plates, as has been shown already by numerical models of subduction in the work by *Capitanio et al.* [2007, 2009]. The fact that no correlation between slab age and dip has been observed [*Goes et al.*, 2011; *Sdrolias and Müller*, 2006] implies then that our 2D models cannot reproduce entirely real subduction settings characterized by further complexities such as, for example, lateral stresses, regional mantle flow, and interaction with other subduction systems.

[23] After reaching the 660 km discontinuity, subduction of young and sub-vertical oceanic plates nearly stops because there is little slab negative buoyancy. As a consequence, the deformation rate

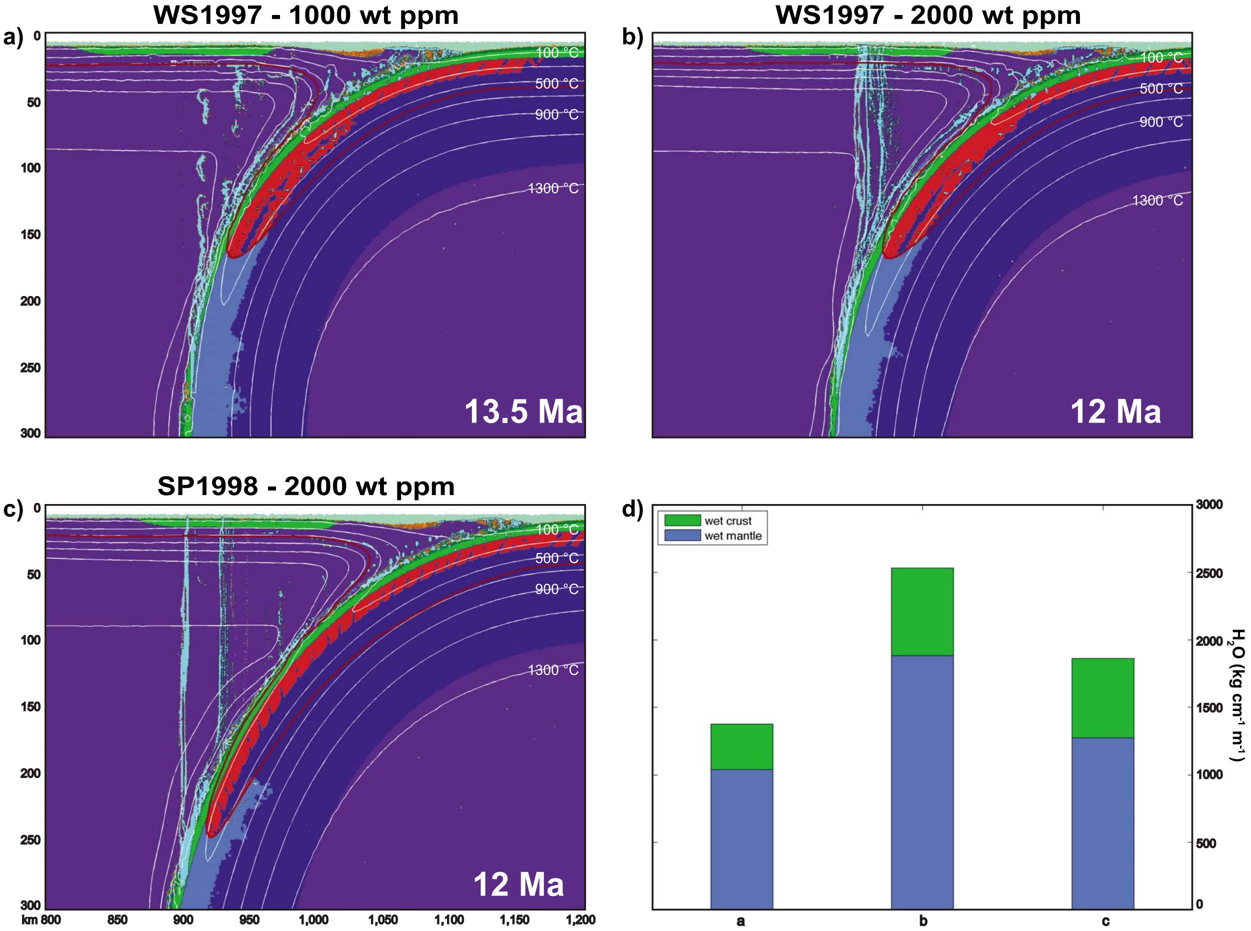

**Figure 6.** Snapshots of numerical models with a different antigorite dehydration curve and degree of oceanic lithosphere wetting with respect to the reference model. (a–c) The dark red lines are the WS1997 and SP1998, while 1000 and 2000 wt ppm indicate the $NAM_{H2O}$ of both the wet oceanic crust and mantle. Color scale as in Figure 3. White lines are isotherms. (d) Volumes of water transported into the transition zone averaged in the 5–15 Ma time window for models in Figures 6a, 6b, and 6c.

is relatively low and slab unbending is not efficient in driving water into the lithospheric mantle. In fact, the lower plane in very young slabs is less than ca.100 km in length (Figures 5a and 5b). In contrast, strong sub-hydrostatic (slab-normal) pressure gradients form in old and stiff oceanic slabs that exhibit a clear and thick DHZ (Figures 5c and 5d). Regardless of whether or not subduction stops, the thickness of the DHZ increases with the slab age (see below). The lower plane of the DHZ forms at temperatures of 500 ± 50°C, except for very young slabs where rehydration of the lithospheric mantle occurs at higher temperatures (Figure 5a).

## 3.3. WS1997 Dehydration Curve

[24] In models shown in Figures 3–5, dehydration of the serpentinized mantle occurs deeper than the maximum depth at which intermediate-depth seismicity is observed in real subduction zones, suggesting that SP1998 probably overestimates the P-T conditions at which dehydration occurs. A similar result has been obtained by *Yamasaki and Seno* [2003], who found a better fit to the observations when using WS1997 (Figure 2). By using such an antigorite dehydration curve, the decomposition of the serpentinized mantle occurs at shallower depths, where slab unbending and sub-hydrostatic (slab-normal) pressure gradients are stronger compared to models using SP1998 (Figures 2 and 3). Consequently, a partially hydrated layer where fluids concentrate forms in the lithospheric mantle more readily and at shallower depths (in the 450 ± 50°C temperature range) with WS1997 (Figures 6a, 6b, 7b, and S3) than with SP1998 (Figures 3, 5, and 6c).

[25] These results show that the downdip extent of the DHZ is quite sensitive to the type of serpentine dehydration curve used because of the large pressure difference at which dehydration occurs.

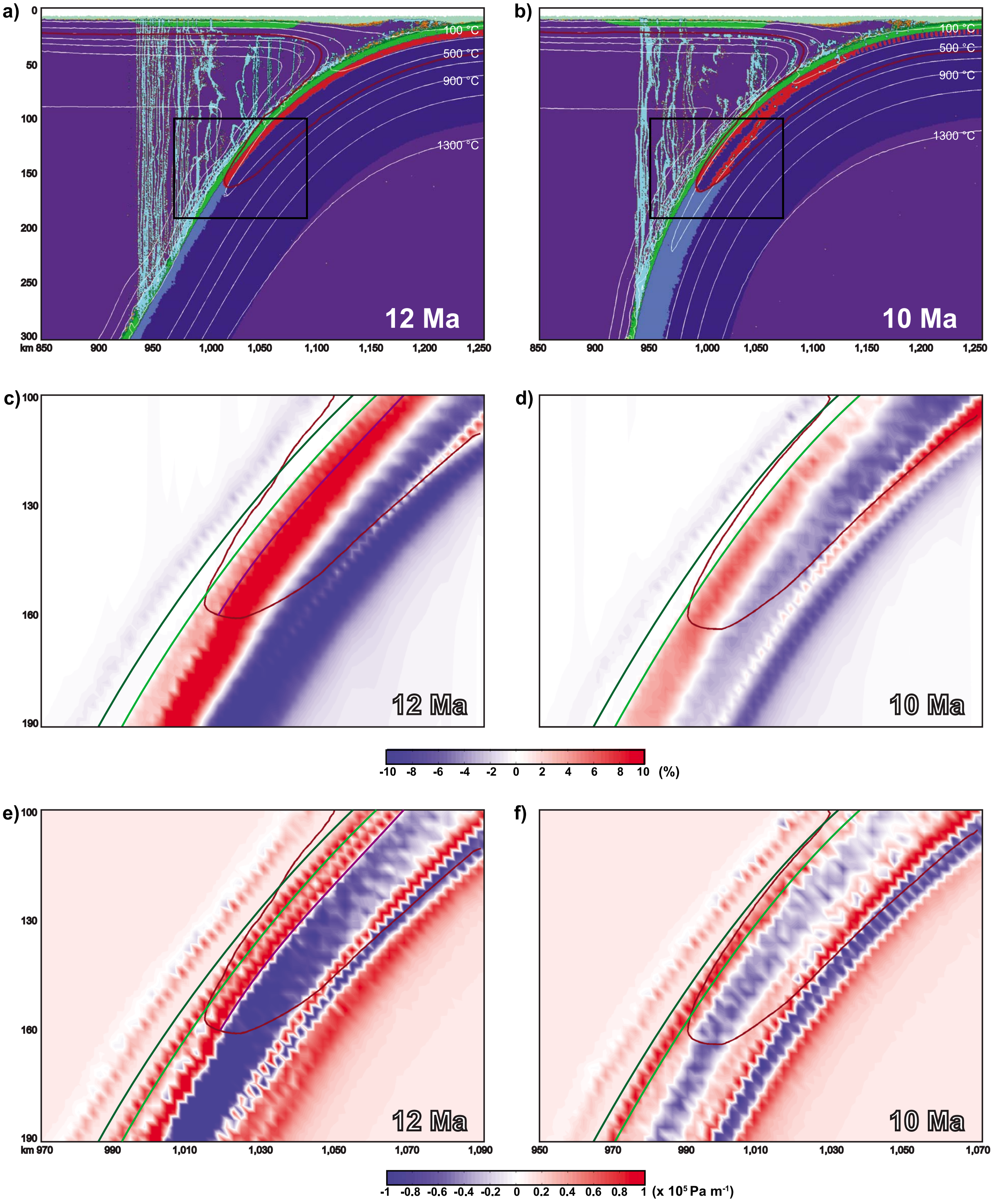
a)
b)
0
50
100
150
200
250
300
km 850
900
950
1,000
1,050
1,100
1,150
1,200
1,250
100 °C
500 °C
900 °C
1300 °C
12 Ma
10 Ma
c)
d)
100
130
160
190
-10 -8 -6 -4 -2 0 2 4 6 8 10 (%)
e)
f)
km 970
990
1,010
1,030
1,050
1,070
1,090
950
970
990
1,010
1,030
1,050
1,070
-1 -0.8 -0.6 -0.4 -0.2 0 0.2 0.4 0.6 0.8 1 (x 10$^5$ Pa m$^{-1}$)

**Figure 7**

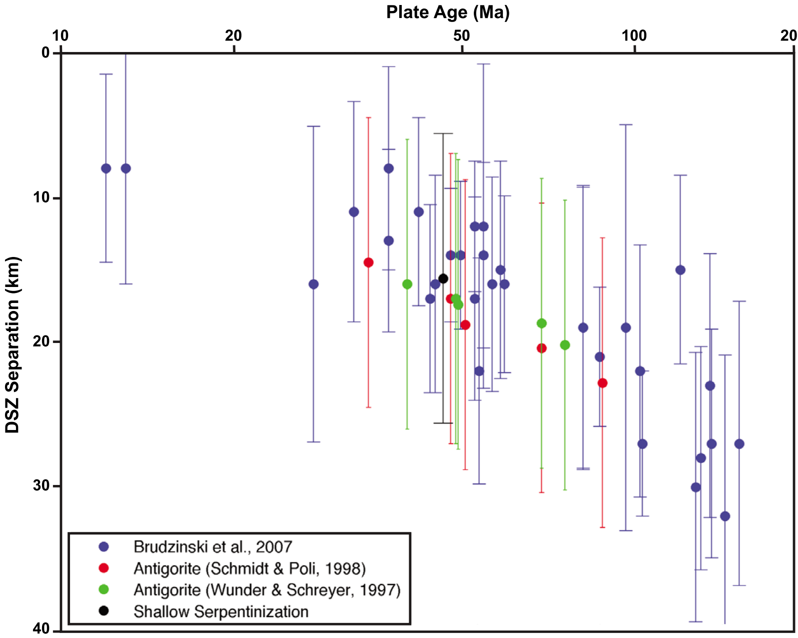

**Figure 8.** Slab-normal DSZ thickness vs plate age at intermediate depths. DSZ thicknesses are measured from the middle of the oceanic crust to the level where fluids concentrate. The 10 km error bars are uncertainties including the thickness of the oceanic crust and of the underlying serpentinized mantle layer, and the variation of the DSZ thickness with depth and time. Blue dots are data from *Brudzinski et al.* [2007]. Red and green dots are data relative to models where the antigorite dehydration curves in Figure 2 have been used. The DSZ of models with a shallow mantle serpentinization at the trench (Figure 7b) is slightly thinner (black dot) because the tectonic over- and under-pressure levels in the rheologically stiffer plate are shifted closer to the Moho.

In fact, at high confining pressures WS1997 has a very small and negative slope compared with SP1998 (Figure 2). On the other hand, the DHZ thickness, and thus the amount of water carried down to the transition zone, is roughly the same for the two sets of models (Figures 6, 8, and 9). This is because the DHZ thickness is mostly sensitive to the thermal structure of the slab and not to the maximum temperature at which antigorite is stable.

## 3.4. Higher Water Content in Nominally Anhydrous Minerals

[26] At depths where the slab dehydrates, the $NAM_{H2O}$ of the wet oceanic crust and mantle is probably higher than the 1000 wt ppm used in our reference model [*Bolfan-Casanova*, 2005; *Mainprice*, 2007]. We therefore also carried out numerical simulations with 2000 wt ppm of water (Figures 6b and 6c). During mantle wetting, more water released by the decomposition of antigorite is consumed and less fluid in excess is available for lithospheric mantle rehydration. As a result, a clear serpentinized layer develops only when using WS1997 (Figure 6b). This is because mantle dehydration occurs at depths where a more efficient slab-inward fluid-flow is established when compared to the model using SP1998 (Figure 6c). The amount of water transported into the transition zone by the model in Figure 6a is roughly the same as for the reference model, while volumes up to 2500 kg

**Figure 7.** Snapshots of numerical models with a shallower mantle serpentinization depth with respect to the reference model. (a) Mantle serpentinization occurs in response to bending-related brittle normal faulting as in the previous models. A homogeneous serpentinized layer forms in the sub-Moho mantle. (b) Mantle serpentinization is imposed heterogeneously along 2 km wide and 5 km long areas spaced 2 km apart. Color scale as in Figure 3. White lines are isotherms. Black boxes delimit the areas shown in Figures 7c, 7d, 7e, and 7f. (c, d) Tectonic pressure map. Values are variations (in percentage) of the total solid pressure relative to the lithostatic load. (e, f) Non-hydrostatic pressure gradient maps rotated in the direction normal to the slab dip. Blue corresponds to sub-hydrostatic pressure gradients, while red indicates fluid supra-hydrostatic gradients. The dark red line is the WS1997. The light and dark green lines are, respectively, the Moho and the top of the gabbroic oceanic crust. The dark purple lines in Figures 7c and 7e mark the bottom of the serpentinized mantle.

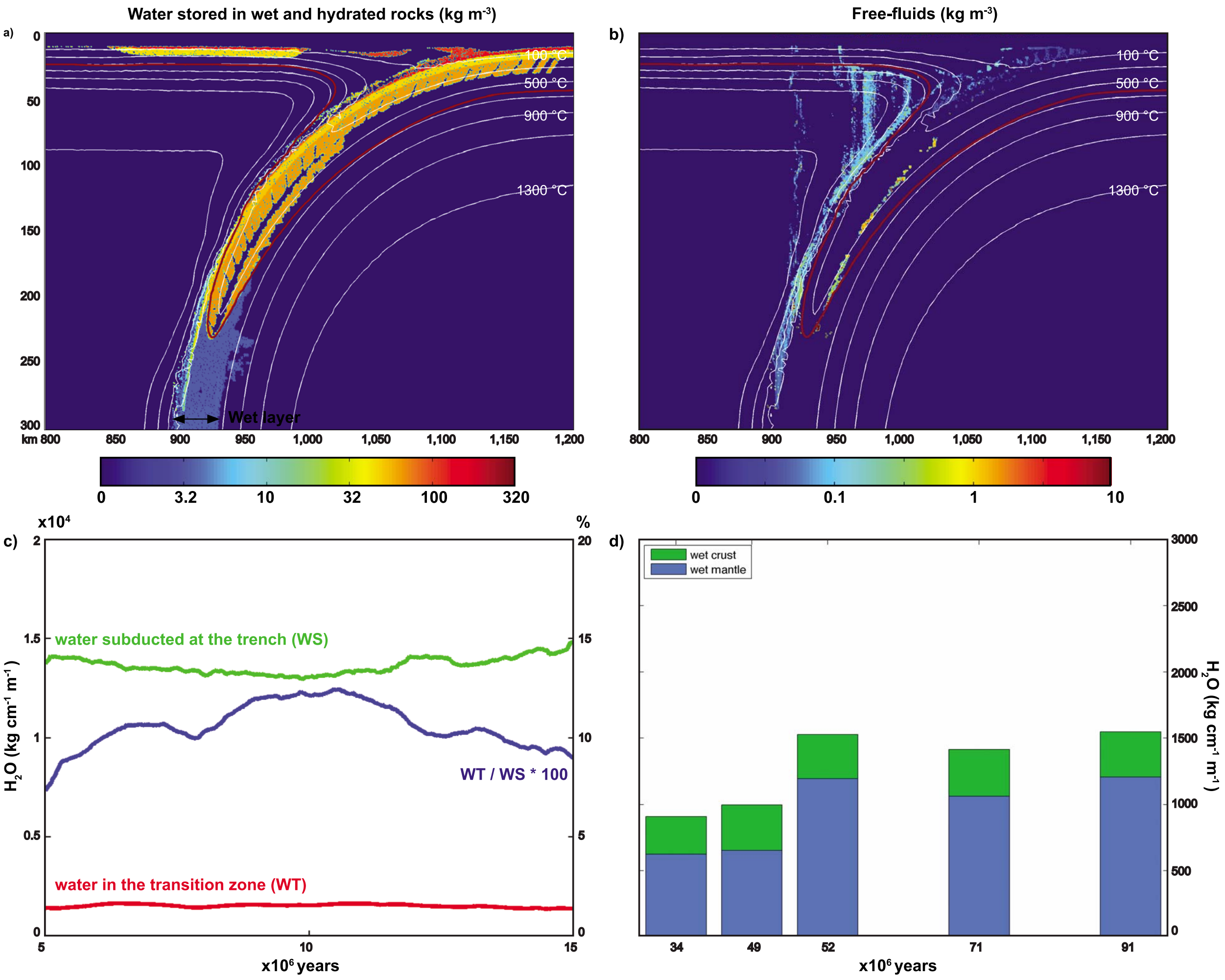

**Figure 9.** Water budget in the subduction zone. Data from the reference model (Figure 3). (a) Water stored in hydrous phases or in nominally anhydrous minerals and (b) free-fluid concentration of Figure 3e. White lines are isotherms. The dark red line is the SP1998 (Figure 2). (c) Total water budget. The green and red lines are volumes of bound water (in kg per cm of subduction per unit length of trench, left axis) entering the subduction zone (50 km leftward of the trench) and the transition zone (400 km depth), respectively. The blue line is the percentage of water transported into the transition zone (right axis). 90% of the water subducted at trenches is returned back to the surface (see also Figure 10). (d) Volumes of water transported into the transition zone (red curve of Figure 9c for the middle column) averaged in the 5–15 Ma time window for models with different initial ages of the subducting slab.

of water per cm of subduction per m of trench are transported down to the transition zone in models where the $NAM_{H2O}$ is 2000 wt ppm (Figure 6d).

[27] This simple comparison of two models with different $NAM_{H2O}$ shows that high $NAM_{H2O}$ can still lead to the formation of a DHZ with, at the same time, a much greater mantle regassing rate. It follows that a more complete database for the water content in nominally anhydrous phases would be useful in future to better estimate how much water can be stored in the wet portion of the slab and how efficiently mantle regassing may occur.

## 3.5. Shallow Serpentinization at the Trench

[28] We further tested the occurrence of a partially hydrated, low velocity mantle layer in models where serpentinization of the slab at trenches is set to occur down to a maximum sub-Moho depth of 5 km (13 km from the slab surface) (Figure 7). The widespread deformation due to bending-related normal faulting induces the formation of a homogeneous, 5 km thick, serpentinized mantle layer (Figure 7a). At depths where the slab mantle dehydrates, the peak of tectonic overpressure (i.e., the slab "watershed") localizes at the base of such a weak layer in

the rheologically strong core of the slab (Figure 7c). As a result, water is expelled upward, driven by fluid supra-hydrostatic gradients (Figure 7e), and no DHZ forms (Figure 7a). In contrast, when shallow but heterogeneous mantle serpentinization is present, a serpentinized lower layer in the slab mantle forms (Figure 7b), because the peak tectonic overpressure localizes closer to the Moho (Figure 7d) and sub-hydrostatic pressure gradients are established between the rheologically strong (dry mantle) and weak (serpentinized mantle) areas of the sub-Moho mantle (Figure 7f). Therefore, since geophysical surveys at trenches [*Ranero et al.*, 2003] and numerical models [*Faccenda et al.*, 2009] have shown that slab hydration occurs heterogeneously along bending-related normal faults, DHZs should also form in subduction zones where shallow mantle serpentinization is detected at the trench.

[29] Comparing these two models at a larger scale (Figures S2a and S2b), it is interesting to note also that the formation of a DHZ enhances slab bending at the 660 km discontinuity and, as a direct consequence, the rate of subduction. This suggests that lithospheric mantle wetting at intermediate depths may cause considerable weakening of the oceanic lithosphere. In fact, this may be a further complexity that should be included in the analysis of subduction zones [e.g., *Goes et al.*, 2011; *Schellart et al.*, 2007; *Sdrolias and Müller*, 2006].

## 3.6. Higher Resolution

[30] Tests of the influence of increased model resolution indicate that the results at higher resolution remain similar to those for the reference model. Figure S3 summarizes the evolution of models with higher resolution (1 km) in the dehydrating region compared to the reference model (2 km). The DHZ is readily formed before the slab reaches the 660 km discontinuity (Figure S3a). The whole upper part of the lithospheric mantle is subsequently serpentinized because of the stress fluctuations induced by slab deformation at the 660 km discontinuity (Figure S3b), after which steady state deformation is achieved, leading to the formation of a DHZ (Figures S3c and S3d). What is different from lower resolution models is that the lower plane of the DHZ rarely merges with upper one.

[31] The higher resolution used in these tests may not yet be sufficient to fully resolve the fluid flow in detail and models with a much higher resolution (tens or hundreds of meters in the dehydrating region) would probably be needed to more robustly confirm our results. However, due to our current computational limits, the resolution could not be increased further.

# 4. Discussion

[32] All the models show that fluids, when released in regions with sub-hydrostatic (slab-normal) pressure gradients, systematically tend to accumulate in a partially hydrated layer located in the 500 ± 50°C temperature range (450 ± 50°C if WS1997 is used) and at a depth below the slab surface that increases with the age of the plate (Figure 8). Such a layer also forms when more fluids are consumed by nominally anhydrous minerals with a higher water solubility ($NAM_{H2O}$ = 2000 wt ppm), provided that mantle dehydration occurs at depths where sub-hydrostatic fluid pressure gradients are present (Figure 6). The formation of a DHZ is favored by WS1997 because antigorite dehydration occurs at depths where deviatoric stresses due to slab unbending are the greatest. Formation of sub-hydrostatic (slab-normal) fluid pressure gradients that drive the water slab-inward is conditional upon the heterogeneous serpentinization of upper mantle in the oceanic plate before it is subducted. However, it is not so dependent on the depth to which the mantle rocks are actually hydrated (Figure 7). In models with only shallow serpentinization due to bending of the plate at the trench (Figure 7b), the serpentinized lower layer is, in a slab-normal profile, somewhat shallower compared to models with deeper serpentinization (Figure 8), indicating that the higher deviatoric stress levels are shifted closer to the surface in poorly hydrated and stiffer oceanic plates.

[33] These results have several implications for the observed intermediate-depth seismicity, the Earth's water budget and slab rheological behavior.

## 4.1. Intermediate-Depth Seismicity

[34] Intermediate-depth seismicity focuses along two dipping planes that form the Double Seismic Zones (DSZs) observed in most subduction zones [*Brudzinski et al.*, 2007]. The distance between the upper and lower planes of DSZs has been shown to be roughly proportional to the slab age, ranging from 8 km for a 12 Ma old slab to 30 km for a 160 Ma old slab. Because of the high confining pressures involved (2–7 GPa), dehydration embrittlement of hydrated crust and mantle in subducting oceanic plates is commonly invoked to explain the seismicity localized in the upper and lower planes of DSZs [e.g., *Kirby et al.*, 1996; *Peacock*, 2001;

*Raleigh and Paterson*, 1965]. Thermal models coupled with petrological databases support such an explanation, showing a good correspondence between the location of the main dehydration reactions and the distribution of the hypocenters [*Hacker et al.*, 2003; *Peacock*, 2001; *Yamasaki and Seno*, 2003].

[35] High-resolution seismological studies carried out with double difference tomography [*Zhang and Thurber*, 2003] seem to confirm the "wet" nature of DSZs. For example, the upper and lower planes of the DSZs under northeast Japan, New Zealand, Central America and southern Italy are associated with lower seismic velocities typical of a partially hydrated oceanic lithosphere and are separated by a region with high seismic velocities [*Caló et al.*, 2009; *Dorbath et al.*, 2008; *Nakajima et al.*, 2009; *Syracuse et al.*, 2008; *Zhang et al.*, 2004]. In particular, low Vp/Vs ratios in the lower plane of the DSZ have been interpreted as due to the presence of free water [e.g., *Takei*, 2002]. *Dorbath et al.* [2008] came to a similar conclusion for northern Chile. They first calculated that the lower plane of seismicity of the Nazca plate is at temperatures of 400 ± 50°C, which are well below the breakdown of hydrous minerals (>500°C), and argued that this layer may correspond to a level of neutral tectonic pressure where fluids from the surrounding dehydration reactions remain trapped during slab unbending.

[36] This interpretation requires that hydrated rocks and fluids must be present in both the crust (upper plane of DSZs) and mantle (lower plane of DSZs) of the subducting slab. However, although DSZs can be as thick as 20–30 km in plates older than 100 Ma [*Brudzinski et al.*, 2007], geophysical surveys at trenches indicate that slab hydration occurs down to a maximum depth of 10–20 km [*Contreras-Reyes et al.*, 2011; *Ivandic et al.*, 2010; *Ranero and Sallares*, 2004]. The most striking example is below northeast Japan, where seismological observations detected one low velocity layer, 10 km thick, in the subducting Pacific plate below the forearc [*Nakajima et al.*, 2009], whereas there are two low velocity (and seismogenic) layers spaced 30 km apart at 50–200 km depth [*Igarashi et al.*, 2001; *Zhang et al.*, 2004]. Furthermore, while *Brudzinski et al.* [2007] showed that the thickness of DSZs is proportional to the slab age, there is no direct relationship between the maximum depth of the hydration at the trench and the age of the subducting plate.

[37] How then is it possible to bring fluids into the lower planes of DSZs in old plates and, more generally, to a depth below the slab surface that is proportional to the age of the oceanic plate? The development of a DHZ is a robust feature in our models that could well explain the relationship between slab age and DSZ thickness [*Brudzinski et al.*, 2007]. In fact, fluids tend systematically to accumulate and migrate in a partially hydrated, low velocity channel with neutral pressure gradients but high deviatoric stresses, located in the 450–500 ± 50°C temperature range and at a depth below the slab surface that increases with the age of the plate (Figure 8). Regardless of the antigorite reaction curve used, the position of the layer where water concentrates is, in a slab-normal profile, always shallower compared to the level of antigorite dehydration. Bearing in mind the uncertainties in both the numerical model parameters, the fluid flow model assumptions and the petrological/geophysical data, this suggests that intermediate-depth earthquakes on the lower plane of DSZs could be mainly triggered by water percolating from deeper or surrounding regions rather than by local dehydration reactions. Differently from the DHZs obtained in the models, DSZ do not seem to merge at around 60 km depth. This may be partly due to the numerical resolution of our models, since those models with a closer Eulerian grid spacing (1km) show no merging of the DHZ (Figure S3).

[38] The DHZ seems to be consistent also with seismic observations where the upper and lower planes of seismicity with low seismic velocities are separated by a dry layer with high seismic velocities. The low Vp/Vs ratios found in the lower plane of DSZs could be attributed to the presence of free fluids in pores [*Takei*, 2002] and/or to the development of seismic anisotropy due to preferentially oriented fluid-filled cracks [*Faccenda et al.*, 2008; *Healy et al.*, 2009] and phyllosilicates [*Mookherjee and Capitani*, 2011], in a manner analogous to that proposed by *Reynard et al.* [2010].

[39] It is worth noting that there is another interpretation proposed for the observed intermediate-depth seismicity and low Vp/Vs ratios of the lower plane of DSZs, which favors a dry lithospheric mantle. In this interpretation, intermediate-depth seismicity is related to ductile shear-heating instabilities developing along pre-existing, fine-grained shear zones [*Kelemen and Hirth*, 2007], while low Vp/Vs ratios are attributed to the anisotropic fabric that could develop in such shear zones [*Reynard et al.*, 2010]. There are some concerns about the inferred mechanisms, because of (1) difficulties in obtaining such shear instabilities in the laboratory and (2) the fact

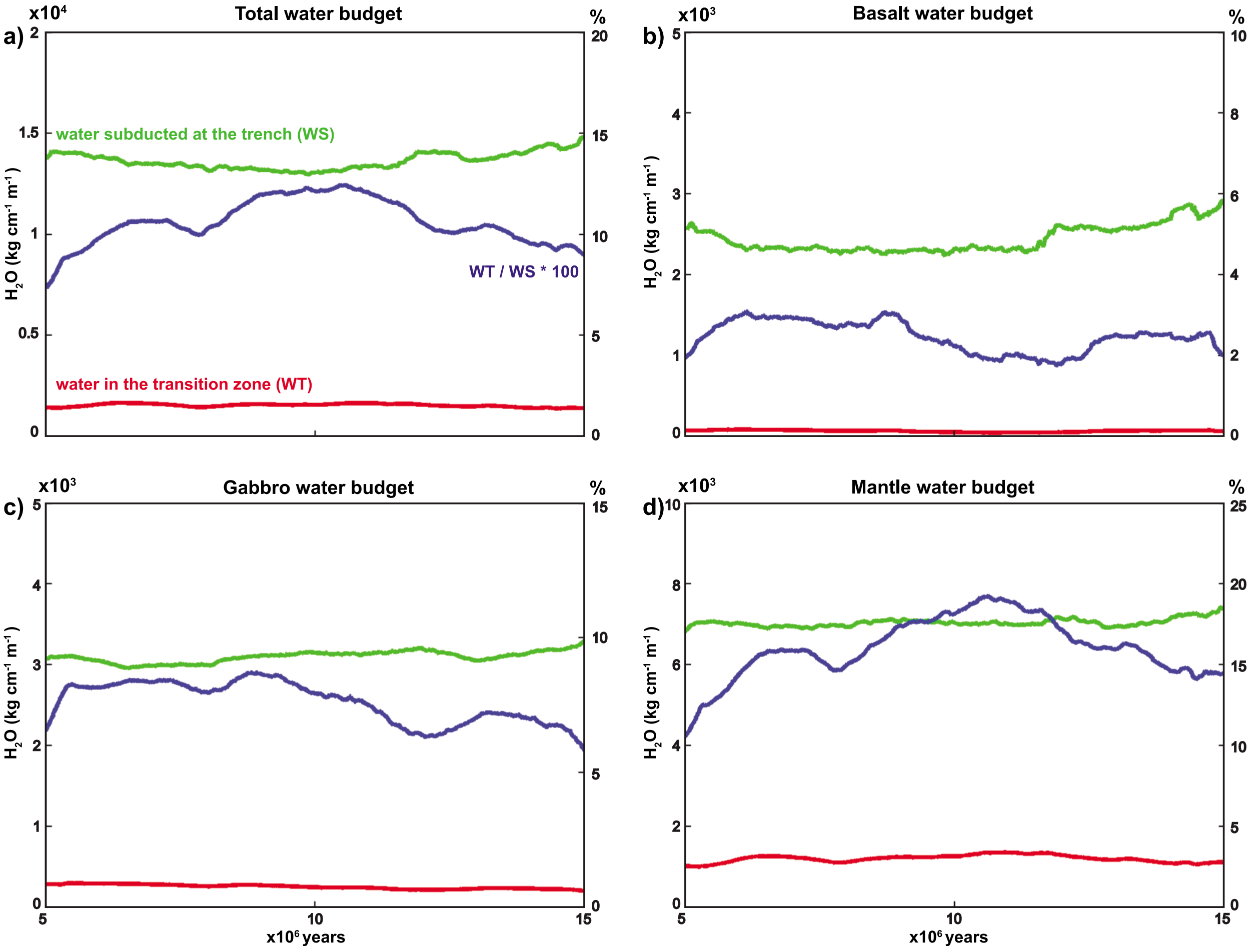

**Figure 10.** Volumes of water transported into the transition zone averaged in the 5–15 Ma time window for the reference model. (a) Total water budget (same as Figure 9c). (b–d) Water budget for basaltic, gabbroic and mantle rocks, respectively. The green and red lines are volumes of bound water (in kg per cm of subduction per m of trench, left axis) entering the subduction zone (50 km leftward of the trench) and the transition zone (400 km depth), respectively. The blue line is the percentage of water transported into the transition zone (right axis).

that the strain in the weakly deforming (unbending) slab is probably not sufficient to produce anisotropic fabrics strong enough to cause the observed low Vp/Vs [*Reynard et al.*, 2010]. However, this interpretation has the attraction that it does not require slab hydration at deep levels. Further seismological and laboratory data may hopefully provide constraints on the degree of hydration along the lower plane of seismicity and help distinguish between the alternative models. For example, receiver function (RF) techniques could be used to reveal the different layers in the downgoing slab [e.g., *Tonegawa et al.*, 2008; *Kawakatsu et al.*, 2009], provided the resolution of the method is high enough to distinguish thin layers with anomalous seismic velocities such as the lower plane of the DSZ. In particular, transverse RF is considered to be usable to detect Ps phases converted at dipping layers.

## 4.2. Earth Water Budget

[40] Subduction of the wet upper portion of the slab also has implications for the deep water cycle and mantle regassing. In our models, oceanic plates carry 1000–2500 kg of water per cm of subduction per m of trench down to the transition zone, which is around 10–20% of the chemically bound water stored at the surface, depending on the slab age and on the $NAM_{H2O}$ (Figure 6d and Figures 9–11). Integrating these values over the past 4.5 billion years and assuming an average subduction rate of 5.5 cm/yr for about 50000 km of trench [*Heuret and Lallemand*, 2005] would mean that the volume of

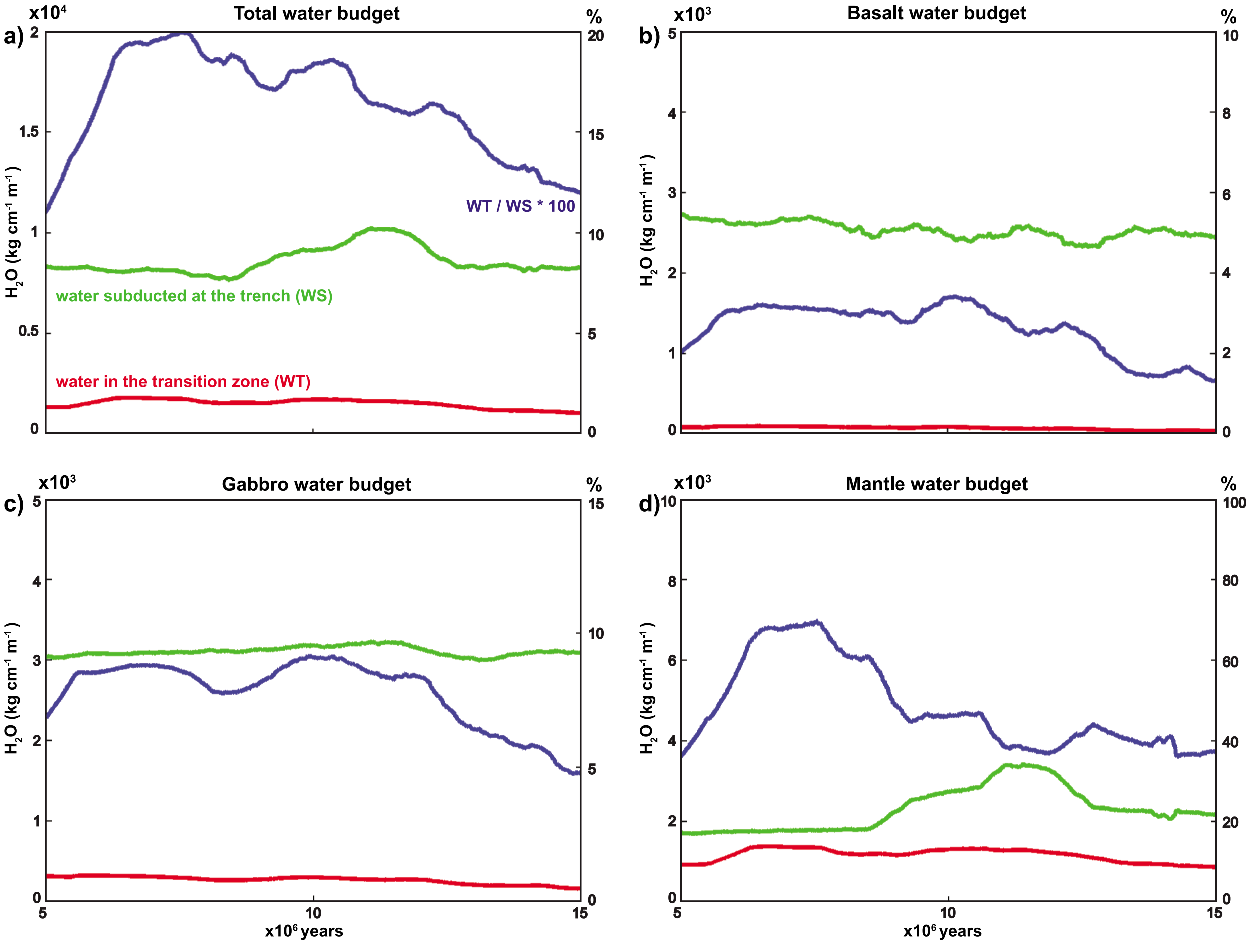

**Figure 11.** Volumes of water transported into the transition zone averaged in the 5–15 Ma time window for the model with shallow and heterogenous serpentinization (Figure 7b). The graphs are computed as described in Figure 10. The amount of water subducted at the trench is about half of that of the reference model (Figure 10a). The water budgets computed for the basaltic and gabbroic crust are the similar to those in Figure 10, while water budget for the lithospheric mantle shows that around 40–70% of water stored by serpentinization is transported down to the transition zone (note that the right axes of Figure 11d is different from Figure 10d).

volatiles contained in around 0.7 to 2 oceans has been carried down to the transition zone during the whole Earth's history, entirely by nominally anhydrous minerals. Though these estimations are comparable with those of *van Keken et al.* [2011], it is worth noting that we did not take into account the formation of Dense Hydrous Magnesium Silicate (DHMS) phases occurring in cold plates. It follows that recycling of water in the deep Earth interior could have been significant through the whole history of our planet without the need for DHMS phases. This interpretation is consistent with mantle-plume-derived basalts with a HIMU source that are low in water (~600 ppm $H_2O$ [*Dixon et al.*, 2002]), and, more generally, with a subducting slab in which water is distributed in small quantities over a large volume.

[41] The total amount of water subducted at the trench for a model with shallow serpentinization occurring at the trench (Figure 11a) corresponds to about $2 \cdot 10^9$ Tg/Ma for present-day subduction zones, consistent with the estimates of *Hacker* [2008] and *van Keken et al.* [2011]. In contrast, models with deeper mantle serpentinization probably overestimate the volumes of subducted water (corresponding to about $3.5 \cdot 10^9$ Tg/Ma, Figure 10a). Interestingly, though the amount of bound water subducted is ~3.5 times smaller than that of models with more extensive serpentinization (compare green lines of Figures 10d and 11d), the volumes of fluids carried into the transition zone are of the same order (red lines of Figures 10d and 11d), meaning that mantle regassing is efficient even when the lithospheric mantle serpentinization at the trench is

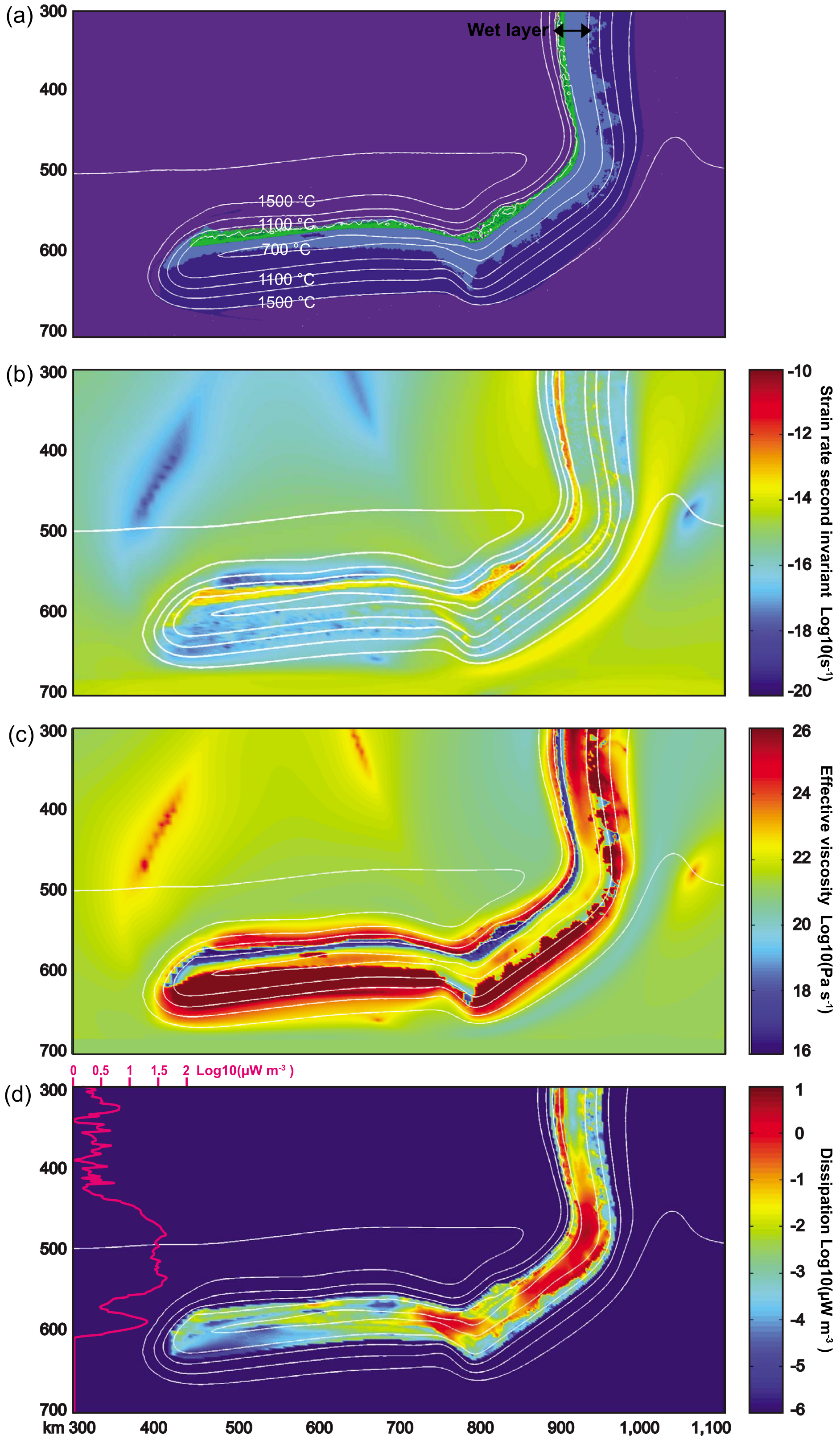

**Figure 12.** Rheological weakening and dissipation in the lower part of the upper mantle for the reference model (Figure 3e). (a) Compositional map. Color scale as in Figure 3. White lines are isotherms. (b) Strain rate map. (c) Effective viscosity. (d) Heat dissipation for material at T < 1000°C. The purple line on the right is the heat dissipation calculated for horizontal layers at various depths.

confined to shallow depths. This is because the thickness of the DHZ is about the same in models with shallow and deep serpentinization (compare Figures 3 and 7b). In fact, the amount of water delivered to the transition zone seems to be proportional to the slab age (Figure 9d) and, hence, to the DSZ thickness, and not to the extent of lithospheric mantle serpentinization occurring at the trench.

[42] Deep subduction of about 1000–2500 kg of water per cm of subduction per m of trench down to the transition zone would also imply 460–1160 m of Phanerozoic sea level drop. *Haq and Schutter* [2008] calculated a sea level variation of about 200 m in the last 550 Ma, meaning either that our data overestimate the regassing rates or that mantle degassing occurring at rifting margins and/or during massive eruptions (such those forming large igneous province) buffered the ocean volume.

### 4.3. Rheological Behavior

[43] The redistribution of water in the zone of slab unbending leads to the formation of a wet (1000–2000 ppm %) layer as thick as the DHZ in the upper and rheologically stronger part of the slab (e.g., Figures 3 and 12). Wetting of ultramafic rocks induces significant rheological weakening, reducing by 1 to 3 orders of magnitude the viscosity [*Karato and Wu*, 1993; *Mei and Kohlstedt*, 2000] and by around 3 times the Peierls stress [*Katayama and Karato*, 2008] of nominally anhydrous minerals. It follows that most of the ductile deformation is expected to occur in the upper 20–30 km of the slab mantle. Figure 12 shows that when the slab bends at the 660 km discontinuity most of the deformation and energy dissipation is concentrated in the wet and weak, upper layer of the slab. It is important to highlight that it is the strong and cold core of the slab that is weakened by wetting, and therefore that the strength of the oceanic plate may be considerably reduced at depth. In fact, compared with oceanic plates characterized by little wetting and weakening (Figure S2a), wetting of the slab cold core due to the formation of the DHZ favors bending at the 660 km discontinuity that, in turn, speeds up subduction (Figure S2b).

## 5. Conclusions

[44] Thermomechanical modeling of slab dehydration coupled with phase transformations and incompressible aqueous fluid flow indicates that part of the volatiles released in the dehydrating subducted lithospheric mantle may flow slab-inward into a region of low total solid pressure. This mechanism leads to the formation of a DHZ where two hydrated layers are separated by a dry region whose thickness increases with the oceanic plate age. The upper and lower planes of the DHZ are characterized by the presence of free fluids and hydrous minerals that may induce deep seismicity and decrease the seismic velocities. The DSZ observed in many subduction zones could be then explained with the formation of a DHZ during slab dehydration because the intermediate-depth hypocenters of the upper and lower planes of DSZs are frequently associated with low seismic velocities anomalies. This interpretation has the advantage that extremely deep plate hydration prior to subduction is not needed to explain thick DSZs in old plates because fluids produced by the breakdown of relatively shallow hydrous phases will reach the deeper portions of the slab during unbending. The occurrence of the lower plane of seismicity seems to depend strictly on the formation of sub-hydrostatic (slab-normal) pressure gradients at depths where mantle dehydration occurs and on fluid availability. It is worth noting that water percolates updip along a plane of neutral (slab-normal) tectonic pressure gradients and not in a plane of neutral tectonic pressure, as previously suggested [*Dorbath et al.*, 2008]. According to our results, intermediate-depth seismicity of DSZs could be explained solely by hydrofracturing. However, we do not exclude a priori other possible triggering mechanisms, such as ductile shear instabilities nucleating in dry and/or hydrated rocks [e.g., *Kelemen and Hirth*, 2007].

[45] Because at depths >300 km the upper 20–30 km of the oceanic plate are wetted by the absorption of fluids in nominally anhydrous minerals, our models show that water can be transported more readily into deeper portions of the upper mantle than previously thought and that significant slab weakening may occur in the strong and cold core of the oceanic plate, facilitating slab bending at the 660 km discontinuity. We estimate that during the whole Earth's history a volume of volatiles contained in about 1 to 2 oceans can be subducted down to the transition zone by solely nominally anhydrous minerals. This suggests that significant mantle regassing could be established even without the formation of high pressure hydrous minerals (DHMS phases) in cold slabs.

[46] Taken together with the previous study of *Faccenda et al.* [2009], these results confirm the important role played by tectonic pressure in driving fluid flow during rock deformation, especially in the bending and unbending regions

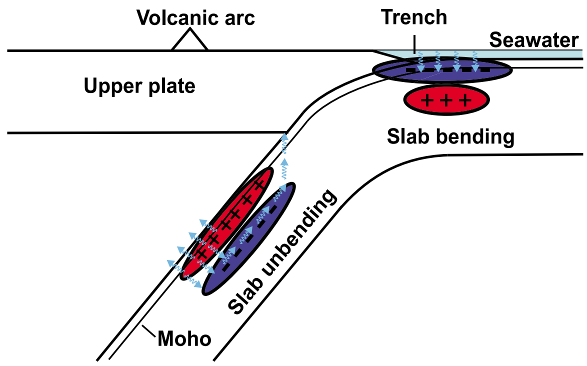

**Figure 13.** Cartoon showing fluid flow driven by tectonic pressure in the bending and unbending areas.

(Figure 13). In the bending area, seawater is pumped downward into the extending portion of the slab along normal faults in which tectonic pressure is lower and permeability is higher compared to the surrounding and poorly deforming rocks [*Faccenda et al.*, 2009]. In contrast, in the unbending area fluids released from the dehydrating slab are driven away from the compressing and over-pressurized upper plane of the slab either toward the mantle wedge or into the slab interior.

## Appendix A

[47] The equations for the conservation of the mass and momentum of a coupled two-phase flow system are [*Spiegelman and McKenzie*, 1987]

$$\frac{\partial \rho_f \phi}{\partial t} + \nabla\cdot(\rho_f \phi v_f) = \Gamma \qquad \text{(A1)}$$

$$\frac{\partial \rho_s (1-\phi)}{\partial t} + \nabla\cdot(\rho_s (1-\phi) v_s) = -\Gamma \qquad \text{(A2)}$$

$$\nabla P_f = \nabla\cdot\eta_s\left(\nabla v_s + \nabla v_s^T\right) + \nabla\cdot\left(\eta_b - \frac{2}{3}\eta_s\right)\nabla\cdot v_s + \bar{\rho} g \qquad \text{(A3)}$$

$$\phi\left(v_f - v_s\right) = -\frac{K}{\eta_f}\nabla \bar{P}_f \qquad \text{(A4)}$$

where $\Gamma$ is mass transfer function between the solid and fluid phases, $\bar{\rho} = \rho_s(1-\varphi) + \varphi\rho_f$ is the density of the mixture and $\eta_b$ is the solid bulk viscosity for compaction (see Table 1 for other symbols explanation).

[48] With constant porosity, no mass transfer and negligible density time derivatives (i.e., using the Boussinesq approximation), the mass conservation equations (A1) and (A2) reduce to those for incompressible fluid and solid phases:

$$\nabla\cdot v_f = 0. \qquad \text{(A5)}$$

$$\nabla\cdot v_s = 0 \qquad \text{(A6)}$$

Furthermore, assuming fluid pressure equal to the solid pressure ($P_f = P_s$, see section 2.1 for a discussion about this and other assumptions made in this derivation) and with $\rho_s \cong \rho_s(1-\varphi) + \varphi\rho_f$ for the small, constant porosity used here (0.01, see Table 1), equation (A3) reduces to the incompressible Stokes equation for a single solid phase:

$$\nabla P_s = \nabla\cdot\eta_s\left(\nabla v_s + \nabla v_s^T\right) + \rho_s g \qquad \text{(A7)}$$

Solving equations (A6) and (A7) for $v_s$ and $P_s$ and noting that the non-hydrostatic (piezometric) fluid pressure gradient in A1.4 is $\nabla\bar{P}_f = \nabla P_f - \rho_f g = \nabla P_s - \rho_f g$, we can reconstruct the fluid velocity using the Darcy's law:

$$v_f = v_s - \frac{K}{\phi\eta_f}\left(\nabla P_s - \rho_f g\right). \qquad \text{(A8)}$$

## Acknowledgments

[49] M.F. thanks Fabio A. Capitanio and Sergio Zlotnik for discussion about the initial model setup and boundary conditions. Marc Spiegelman and an anonymous reviewer helped in clarifying several concepts and discussions that significantly improved the manuscript. This work has been supported by SNSF fellowship PBEZP2–126187 to M.F.

## References

Babeyko, A. Y., and S. V. Sobolev (2008), High-resolution numerical modeling of stress distribution in visco-elasto-plastic subducting slabs, *Lithos*, *103*, 205–216, doi:10.1016/j.lithos.2007.09.015.

Bercovici, D., and S. Karato (2003), Whole-mantle convection and the transition-zone water filter, *Nature*, *425*, 39–44, doi:10.1038/nature01918.

Bolfan-Casanova, N. (2005), Water in the Earth's mantle, *Mineral. Mag.*, *69*(3), 229–258, doi:10.1180/0026461056930248.

Brudzinski, M. R., C. H. Thurber, B. R. Hacker, and E. R. Engdahl (2007), Global prevalence of double Benioff zones, *Science*, *316*, 1472–1474, doi:10.1126/science.1139204.

Cagnioncle, A.-M., E. M. Parmentier, and L. T. Elkins-Tanton (2007), Effect of solid flow above a subducting slab on water distribution and melting at convergent plate boundaries, *J. Geophys. Res.*, *112*, B09402, doi:10.1029/2007JB004934.

Caló, M., C. Dorbath, D. Luzio, S. G. Rotolo, and G. D'anna (2009), Local earthquake tomography in the Southern Tyrrhenian region of Italy: Geophysical and petrological inferences on the subducting lithosphere, in *Subduction Zone*

*Geodynamics*, edited by S. Lallemand and F. Funiciello, pp. 85–99, Springer, Berlin.

Capitanio, F. A., G. Morra, and S. Goes (2007), Dynamic models of downgoing plate-buoyancy driven subduction: Subduction motions and energy dissipation, *Earth Planet. Sci. Lett.*, *262*(1–2), 284–297, doi:10.1016/j.epsl.2007.07.039.

Capitanio, F. A., G. Morra, and S. Goes (2009), Dynamics of plate bending at the trench and slab-plate coupling, *Geochem. Geophys. Geosyst.*, *10*, Q04002, doi:10.1029/2008GC002348.

Carslaw, H. S., and J. C. Jaeger (1984), *Conduction of Heat in Solids*, 2nd ed., Clarendon, Oxford, U. K.

Clauser, C., and E. Huenges (1995), Thermal conductivity of rocks and minerals, in *Rock Physics & Phase Relations: A Handbook of Physical Constants*, *AGU Ref. Shelf*, vol. 3, edited by T. J. Ahrens, pp. 105–126, AGU, Washington, D. C., doi:10.1029/RF003p0105.

Connolly, J. A. D. (2005), computation of phase equilibria by linear programming: A tool for geodynamical modelling and its application to subduction zone decarbonation, *Earth Planet. Sci. Lett.*, *236*, 524–541, doi:10.1016/j.epsl.2005.04.033.

Connolly, J. A. D., and Y. Y. Podladchikov (2004), Fluid flow in compressive tectonic settings: Implications for midcrustal seismic refractors and downward fluid migration, *J. Geophys. Res.*, *109*, B04201, doi:10.1029/2003JB002822.

Contreras-Reyes, E., I. Grevemeyer, A. B. Watts, E. R. Flueh, C. Peirce, S. Moeller, and C. Papenberg (2011), Deep seismic structure of the Tonga subduction zone: Implications for mantle hydration, tectonic erosion, and arc magmatism, *J. Geophys. Res.*, *116*, B10103, doi:10.1029/2011JB008434.

Dixon, J. E., L. Leist, C. Langmuir, and J.-G. Schilling (2002), Recycled dehydrated lithopshere observed in plume-influenced mid-ocean-ridge basalt, *Nature*, *420*, 385–389, doi:10.1038/nature01215.

Dorbath, C., M. Gerbault, G. Carlier, and M. Guiraud (2008), Double seismic zone of the Nazca plate in Northern Chile: High-resolution velocity structure, petrological implications, and thermomechanical modelling, *Geochem. Geophys. Geosyst.*, *9*, Q07006, doi:10.1029/2008GC002020.

Faccenda, M., and N. Mancktelow (2010), Fluid flow during unbending: Implications for slab hydration, intermediate-depth earthquakes and deep fluid subduction, *Tectonophysics*, *494*(1–2), 149–154, doi:10.1016/j.tecto.2010.08.002.

Faccenda, M., L. Burlini, T. V. Gerya, and D. Mainprice (2008), Fault-induced seismic anisotropy by hydration in subducting oceanic plates, *Nature*, *455*(7216), 1097–1100, doi:10.1038/nature07376.

Faccenda, M., T. V. Gerya, and L. Burlini (2009), Deep slab hydration induced by bending-related variations in tectonic pressure, *Nat. Geosci.*, *2*(11), 790–793, doi:10.1038/ngeo656.

Gerya, T. V., and D. A. Yuen (2003), Rayleigh-Taylor instabilities from hydration and melting propel "cold plumes" at subduction zones, *Earth Planet. Sci. Lett.*, *212*, 47–62, doi:10.1016/S0012-821X(03)00265-6.

Gerya, T. V., and D. A. Yuen (2007), Robust characteristics method for modelling multiphase visco-elasto-plastic thermo-mechanical problems, *Phys. Earth Planet. Inter.*, *163*, 83–105, doi:10.1016/j.pepi.2007.04.015.

Gerya, T. V., J. A. D. Connolly, and D. A. Yuen (2008), Why is terrestrial subduction one-sided?, *Geology*, *36*(1), 43–46, doi:10.1130/G24060A.1.

Goes, S., F. A. Capitanio, G. Morra, M. Seton, and D. Giardini (2011), Signatures of downgoing plate-buoyancy driven subduction in Cenozoic plate motions, *Phys. Earth Planet. Inter.*, *184*(1–2), 1–13, doi:10.1016/j.pepi.2010.10.007.

Gorczyk, W., A. P. Willner, T. V. Gerya, J. A. D. Connolly, and J.-P. Burg (2007), Physical controls of magmatic productivity at Pacific-type convergent margins: Numerical modelling, *Phys. Earth Planet. Inter.*, *163*, 209–232, doi:10.1016/j.pepi.2007.05.010.

Hacker, B. R. (2008), $H_2O$ subduction beyond arcs, *Geochem. Geophys. Geosyst.*, *9*, Q03001, doi:10.1029/2007GC001707.

Hacker, B. R., S. M. Peacock, G. A. Abers, and S. D. Holloway (2003), Subduction factory: 2. Are intermediate-depth earthquakes in subducting slabs linked to metamorphic dehydration reactions?, *J. Geophys. Res.*, *108*(B1), 2030, doi:10.1029/2001JB001129.

Haq, B. U., and S. R. Schutter (2008), A chronology of Paleozoic sea-level changes, *Science*, *322*, 64–68, doi:10.1126/science.1161648.

Healy, D., S. M. Reddy, N. E. Timms, E. M. Gray, and A. Vitale Brovarone (2009), Trench-parallel fast axes of seismic anisotropy due to fluid-filled cracks in subducting slabs, *Earth Planet. Sci. Lett.*, *283*, 75–86, doi:10.1016/j.epsl.2009.03.037.

Hebert, L. B., P. Antoshechkina, P. Asimow, and M. Gurnis (2009), Emergence of a low-viscosity channel in subduction zones through the coupling of mantle flow and thermodynamics, *Earth Planet. Sci. Lett.*, *278*, 243–256, doi:10.1016/j.epsl.2008.12.013.

Heuret, A., and S. Lallemand (2005), Plate motions, slab dynamics and back-arc deformation, *Phys. Earth Planet. Inter.*, *149*(1–2), 31–51, doi:10.1016/j.pepi.2004.08.022.

Igarashi, T., T. Matsuzawa, N. Umino, and A. Hasegawa (2001), Spatial distribution of focal mechanisms for interplate and intraplate earthquakes associated with the subducting Pacific plate beneath the northeastern Japan arc: A triple-planed deep seismic zone, *J. Geophys. Res.*, *106*, 2177–2191, doi:10.1029/2000JB900386.

Ivandic, M., I. Grevemeyer, J. Bialas, and C. J. Petersen (2010), Serpentinization in the trench-outer rise region offshore of Nicaragua: Constraints from seismic refraction and wide-angle data, *Geophys. J. Int.*, *180*, 1253–1264, doi:10.1111/j.1365-246X.2009.04474.x.

Jung, H., H. W. Green, and L. F. Dobrzhinetskaya (2004), Intermediate-depth earthquake faulting by dehydration embrittlement with negative volume change, *Nature*, *428*, 545–549.

Karato, S., and P. Wu (1993), Rheology of the upper mantle: A synthesis, *Science*, *260*, 771–778, doi:10.1126/science.260.5109.771.

Katayama, I., and S. Karato (2008), Low-temperature, high-stress deformation of olivine under water saturated conditions, *Phys. Earth Planet. Inter.*, *168*, 125–133, doi:10.1016/j.pepi.2008.05.019.

Katz, R. F., M. Spiegelman, and B. Holtzman (2006), The dynamics of melt and shear localization in partially molten aggregates, *Nature*, *442*, 676–679, doi:10.1038/nature05039.

Kawakatsu, H., P. Kumar, Y. Takei, M. Shinohara, T. Kanazawa, E. Araki, and K. Suyehiro (2009), Seismic evidence for sharp lithosphere-asthenosphere boundaries of oceanic plates, *Science*, *324*, 499–502.

Kelemen, P. B., and G. Hirth (2007), A periodic shear-heating mechanism for intermediate-depth earthquakes in the mantle, *Nature*, *446*, 787–790, doi:10.1038/nature05717.

Kirby, S., R. E. Engdahl, and R. Denlinger (1996), Intermediate-depth intraslab earthquakes and arc volcanism as physical expressions of crustal and uppermost mantle metamorphism in subducting slabs, in *Subduction Top to Bottom*, *Geophys. Monogr. Ser.*, vol. 96, edited by E. Bebout et al., pp. 195–214, AGU, Washington, D. C., doi:10.1029/GM096p0195.

Kushiro, I., Y. Syono, and S.-I. Akimoto (1968), Melting of a peridotite nodule at high pressures and high water pressures, *J. Geophys. Res.*, *73*, 6023–6029, doi:10.1029/JB073i018p06023.

Mainprice, D. (2007), Seismic anisotropy of the deep Earth from a mineral and rock physical perspective, in *Treatise of Geophysics*, vol. 2, *Mineral Physics*, edited by G. D. Price, pp. 437–491, Elsevier, Boston, Mass., doi:10.1016/B978-044452748-6.00045-6.

Mancktelow, N. (2008), Tectonic pressure: Theoretical concepts and modeled examples, *Lithos*, *103*, 149–177, doi:10.1016/j.lithos.2007.09.013.

Mei, S., and D. L. Kohlstedt (2000), Influence of water on plastic deformation of olivine aggregates, *J. Geophys. Res.*, *105*, 21,457–21,469, doi:10.1029/2000JB900179.

Mookherjee, M., and G. C. Capitani (2011), Trench parallel anisotropy and large delay times: Elasticity and anisotropy of antigorite at high pressures, *Geophys. Res. Lett.*, *38*, L09315, doi:10.1029/2011GL047160.

Nakajima, J., Y. Tsuji, A. Hasegawa, S. Kita, T. Okada, and T. Matsuzawa (2009), Tomographic imaging of hydrated crust and mantle in the subducting Pacific slab beneath Hokkaido, Japan: Evidence for dehydration embrittlement as a cause of intraslab earthquakes, *Gondwana Res.*, *16*, 470–481.

Ohtani, E. (2005), Water in the mantle, *Elements*, *1*, 25–30, doi:10.2113/gselements.1.1.25.

Peacock, S. M. (2001), Are the lower planes of double seismic zones caused by serpentine dehydration in subducting oceanic mantle?, *Geology*, *29*, 299–302, doi:10.1130/0091-7613(2001)029<0299:ATLPOD>2.0.CO;2.

Raleigh, C. B., and M. S. Paterson (1965), Experimental deformation of serpentine and its tectonic implications, *J. Geophys. Res.*, *70*(16), 3965–3985, doi:10.1029/JZ070i016p03965.

Ranalli, G. (1995), *Rheology of the Earth*, Chapman and Hall, London.

Ranero, C. R., and V. Sallares (2004), Geophysical evidence for hydration of the crust and mantle of the Nazca plate during bending at the North Chile trench, *Geology*, *32*, 549–554, doi:10.1130/G20379.1.

Ranero, C. R., J. Phipps Morgan, K. McIntosh, and C. Reichert (2003), Bending-related faulting and mantle serpentinization at the Middle America trench, *Nature*, *425*, 367–373, doi:10.1038/nature01961.

Reynard, B., J. Nakajima, and H. Kawakatsu (2010), Earthquakes and plastic deformation of anhydrous slab mantle in double Wadati-Benioff zones, *Geophys. Res. Lett.*, *37*, L24309, doi:10.1029/2010GL045494.

Rüpke, L. H., J. Phipps Morgan, M. Hort, and J. A. D. Connolly (2004), Serpentine and the subduction zone water cycle, *Earth Planet. Sci. Lett.*, *223*, 17–34, doi:10.1016/j.epsl.2004.04.018.

Schellart, W. P., J. Freeman, D. R. Stegman, L. Moresi, and D. May (2007), Evolution and diversity of subduction zones controlled by slab width, *Nature*, *446*, 308–311, doi:10.1038/nature05615.

Schmidt, M. W., and S. Poli (1998), Experimentally based water budgets for dehydrating slabs and consequences for arc magma generation, *Earth Planet. Sci. Lett.*, *163*, 361–379, doi:10.1016/S0012-821X(98)00142-3.

Sdrolias, M., and R. D. Müller (2006), Controls on back-arc basin formation, *Geochem. Geophys. Geosyst.*, *7*, Q04016, doi:10.1029/2005GC001090.

Seno, T., and Y. Yamanaka (1996), Double seismic zones, compressional deep trench-outer rise events, and superplumes, in *Subduction Top to Bottom*, *Geophys. Monogr. Ser.*, vol. 96, edited by E. Bebout et al., pp. 347–355, AGU, Washington, D. C., doi:10.1029/GM096p0347.

Spiegelman, M., and D. McKenzie (1987), Simple 2-D models for melt extraction at mid-ocean ridges and island arcs, *Earth Planet. Sci. Lett.*, *83*, 137–152, doi:10.1016/0012-821X(87)90057-4.

Syracuse, E. M., G. A. Abers, K. Fischer, L. MacKenzie, C. Rychert, M. Protti, V. González, and W. Strauch (2008), Seismic tomography and earthquake locations in the Nicaraguan and Costa Rican upper mantle, *Geochem. Geophys. Geosyst.*, *9*, Q07S08, doi:10.1029/2008GC001963.

Takei, Y. (2002), Effect of pore geometry on $V_P/V_S$: From equilibrium geometry to crack, *J. Geophys. Res.*, *107*(B2), 2043, doi:10.1029/2001JB000522.

Tonegawa, T., K. Hirahara, T. Shibutani, H. Iwamori, H. Kanamori, and K. Shiomi (2008), Water flow to mantle transition zone inferred from a receiver function image of the Pacific slab, *Earth Planet. Sci. Lett.*, *274*, 346–354, doi:10.1016/j.epsl.2008.07.046.

Van Avendonk, H. J. A., W. S. Holbrook, D. Lizarralde, and P. Denyer (2011), Structure and serpentinization of the subducting Cocos plate offshore Nicaragua and Costa Rica, *Geochem. Geophys. Geosyst.*, *12*, Q06009, doi:10.1029/2011GC003592.

van Keken, P. E., B. R. Hacker, E. M. Syracuse, and G. A. Abers (2011), Subduction factory: 4. Depth-dependent flux of $H_2O$ from subducting slabs worldwide, *J. Geophys. Res.*, *116*, B01401, doi:10.1029/2010JB007922.

Wang, D., M. Mookherjee, Y. Xu, and S.-I. Karato (2006), The effect of water on the electrical conductivity of olivine, *Nature*, *443*, 977–980, doi:10.1038/nature05256.

Wunder, B., and W. Schreyer (1997), Antigorite: High-pressure stability in the system MgO-$SiO_2$–$H_2O$ (MSH), *Lithos*, *41*, 213–227, doi:10.1016/S0024-4937(97)82013-0.

Yamasaki, T., and T. Seno (2003), Double seismic zone and dehydration embrittlement of the subducting slab, *J. Geophys. Res.*, *108*(B4), 2212, doi:10.1029/2002JB001918.

Zhang, H., and C. H. Thurber (2003), Double-difference tomography: The method and its application to the Hayward fault, California, *Bull. Seismol. Soc. Am.*, *93*(5), 1875–1889, doi:10.1785/0120020190.

Zhang, H., C. H. Thurber, D. Shelly, S. Ide, G. C. Beroza, and A. Hasegawa (2004), High-resolution subducting-slab structure beneath northern Honshu, Japan, revealed by double-difference tomography, *Geology*, *32*, 361–364, doi:10.1130/G20261.2.